Fluidically Programmed Wearable Haptic Textiles

Authors

Barclay Jumet,[1] Zane A. Zook,[1] Anas Yousaf,[1] Anoop Rajappan,[1] Doris Xu,[1]
Te Faye Yap,[1] Nathaniel Fino,[1] Zhen Liu,[1] Marcia K. O'Malley,[1,2,3] Daniel J. Preston[1]*

Affiliations

[1]Department of Mechanical Engineering, Rice University, Houston, TX 77005, USA.
[2]Department of Computer Science, Rice University, Houston, TX 77005, USA.
[3]Department of Electrical and Computer Engineering, Rice University, Houston, TX
77005, USA.

*Corresponding author. Email: djp@rice.edu

Summary

Haptic feedback offers a useful mode of communication in visually or auditorily noisy
environments. The adoption of haptic devices in our everyday lives, however, remains
limited, motivating research on haptic wearables constructed from materials that enable
comfortable and lightweight form factors. Textiles—a material class fitting these needs
and already ubiquitous in clothing—have begun to be used in haptics, but reliance on
arrays of electromechanical controllers detracts from the benefits that textiles offer. Here,
we mitigate the requirement for bulky hardware by developing a class of wearable haptic
textiles capable of delivering high-resolution information based on embedded fluidic
programming. The designs of these haptic textiles enable tailorable amplitudinal, spatial,
and temporal control. Combining these capabilities, we demonstrate wearables that
deliver spatiotemporal cues in four directions with an average user accuracy of 87%.
Subsequent demonstrations of washability, repairability, and utility for navigational tasks
exemplify the capabilities of our approach.

Keywords: analog control, fluidic control, smart textiles, point force, tactile cues, navigation,
directional cues, haptic sleeve, spatiotemporal haptics

Context & Scale

Our increasingly connected and information-rich lives demand new modes of
communication. Haptic cues offer many advantages for an on-the-go, always-connected
lifestyle, yet wearable haptic devices often require extensive external hardware to provide
the complex cues required for high-resolution delivery of information. In this work, we
developed and characterized a suite of haptic cues enabled by the textile material
platform that are—as compared to the state of the art—capable of delivering complex
haptic information with simplified infrastructure, robust when subjected to the wear and
tear of everyday life, and able to be tailored to a high degree of specificity in regards to
their haptic outputs (varying in force, time, and space). This work therefore enables
wearable haptic textiles that not only provide complex cues with substantially reduced
hardware but also feel and look like everyday clothing.

MAIN TEXT

Introduction

The sights and sounds encountered in our everyday lives often surpass our limited bandwidth for absorbing and processing information. Haptic sensations, transmitted primarily through our sense of touch, enable a tertiary mode of communication beyond these saturated visual and auditory modes that add to—yet do not clutter—our ability to receive information. Moreover, persons with clinically encumbered visual and auditory senses can benefit from haptic interventions in an otherwise visual- and auditory-centric world, including approximately 1.1 billion people worldwide living with a loss of vision and another 1.5 billion people with a loss of hearing.[1,2] As a consequence, haptic technologies serve as an integral tool for both supplementing and complementing clinically impeded or otherwise saturated modes of conventional communication, especially regarding the navigation of "noisy" environments,[3–5] immersion into augmented or virtual realities,[6–11] human-robot interaction,[12–15] and general assistance throughout our activities of daily living.[16–19]

Haptic stimuli include sensations relating to temperature, pain, and mechanoreception (i.e., forces or pressures applied to the skin); tactile mechanoreceptors in particular represent a proven route for interpreting spatially and temporally distinct cues.[20] For decades, haptics researchers have been deepening our understanding of the relevant psychophysics of haptic perception and have produced a variety of haptic devices capable of delivering tactile cues.[21–23] More recent research into wearable systems strives to translate these haptic devices to comfortable, unobtrusive form factors that could better enable wide societal adoption.[24–38] Nevertheless, soft wearables frequently employ silicone and other elastomeric materials,[39] which can counteractively add bulk and obstruct movement. As an alternative, textile-based wearables can be substantially lighter than their elastomeric counterparts due to their two-dimensional sheet-like form factor (i.e., following an L^2 scaling versus the L^3 scaling of elastomers), and textiles are also more resistant to cuts, tears, and abrasions,[40,41] positioning themselves at a higher "level of wearability," where form factor, weight, impairment to the user, and comfort are the primary considerations.[42] Moreover, society has already adopted textiles as a ubiquitous format for items that interface with humans every day, including clothing, blankets, and furniture. Devices made from the textile material platform are thus not only economically

manufacturable at industrial scales but can also be integrated into many items that we use daily. In recognition of these attributes, textile-based (and, more generally, sheet-based) wearable haptic devices have garnered interest from the haptics community,[43–63] often by simply using textiles to ground conventional rigid haptic devices to a user (table S1). Despite recent progress on sheet- and textile-based haptic actuators in particular, their utility frequently remains limited to relatively simple mechanisms of fluidic actuation in which pressure is transduced to force in isolated bladders, requiring extraneous off-board hardware and diminishing the very benefits that textiles offer. On-boarding the control aspect of these devices while maintaining compliance and light weight would simplify soft wearable haptic devices and allow wider use in real-world scenarios.

Fluidic control provides a method of removing off-board electromechanical components, streamlining the overall system, and unifying the energetic media upon which the controllers and actuators of wearables operate.[64–72] Whereas the benefits of both digital and analog fluidic control have been realized in a host of soft architectures, they are—as with wearable actuators—primarily elastomeric. Following the outlined benefits of textile architectures, digital logic has been explored in textiles,[68] but the porting of analog logic to the textile platform has not yet been demonstrated. Analog control can complement or offer a standalone alternative to digital control,[72–76] further enabling the functionality and consequential adoption of wearables. Yet in the absence of solutions transcribed to a textile format, the translation of the technology to a truly wearable format has remained difficult. Appropriating fluidic analog control to a textile device enables diverse haptic cueing with a reduced system as compared to electronic (or fluidic digital) control, thereby presenting the gap this work fills: the introduction of a paradigm of design to create more capable haptic devices while simultaneously reducing the burden on the user. Here, we incorporate the concepts of analog fluidic control and material intelligence to attain the concomitant benefits of these approaches.[77–82]

In this work, we present a suite of wearable haptic devices made from heat-sealable textiles (HSTs) in the form of wristbands and sleeves that convey information through the wrist or arm. These haptic textiles convey information upon application of pneumatic pressure (Figure 1A) and exhibit (i) amplitude control through geometric design and regulated pneumatic pressure (Figure 1B), (ii) temporal control for a spectrum of cues ranging from continuous constant forces to stepped and periodic oscillations (Figure 1C), and (iii) spatial control through geometric design of the textile layers (Figure 1D). After

characterizing these capabilities individually, we demonstrated spatiotemporal cues (i.e., varying in both position and time) with traditional electronic valve-based control as well as through material-based fluidic programming integrated within the structure of the haptic textiles themselves (Figure 1E), which enables complex spatiotemporal cues (and thus high-resolution information transfer) using only one constant-pressure on-off input, based upon the resistor-capacitor circuits of analog control. The added programmability using simplified control schemes not only enables more pragmatic wearables but also reveals entirely new modes of operation and functionality for tactile haptic cues. Furthermore, we tested the efficacy of our programmed haptic textiles on human participants in a four-direction test, and participants identified cues with an average accuracy of 87% overall and an accuracy of 97% among participants above the median in terms of performance. We also demonstrate the capabilities of our programmed spatiotemporal cues in two untethered navigational tasks: (i) wirelessly guiding a user from waypoint to waypoint on city streets, and (ii) directing a user to draw tetrominoes (shapes created through the orthogonal connection of four unit squares) on an open field. After confirming the haptic efficacy of these programmed fluidic haptic textiles, we showed that they can be used "in the wild" and withstand regular use, including 25 cycles of washing as well as repairing a cut using a patch and a home-use iron, both without any degradation in performance. These demonstrations of efficacy, usability, and durability show how our approach to fluidic haptic textiles, leveraging fluidic programming, can enable real-world use in wearable applications including virtual reality, human-robot interaction, and beyond.

Results

Amplitude Control

Our haptic textiles impart force-based tactile cues through the out-of-plane inflation of integrated inflatable cells located between inextensible textile sheets oriented in-plane with the user's skin (Figure S1). The textile is coated with a thin film of thermoplastic polyurethane (TPU) which creates a thermally bondable fabric. Under the application of heat and pressure, the HSTs form a hermetic (i.e., gas-tight) bond, and a rectangular non-stick intermediate region defines the inflatable cells. The computer-numerical-control (CNC) approach that we used for fabrication enables a diversity of wearable designs, including single-cell bands for the wrist and multi-cell sleeves for the forearm as deployed in this work (Figure 2A and Figure S2).
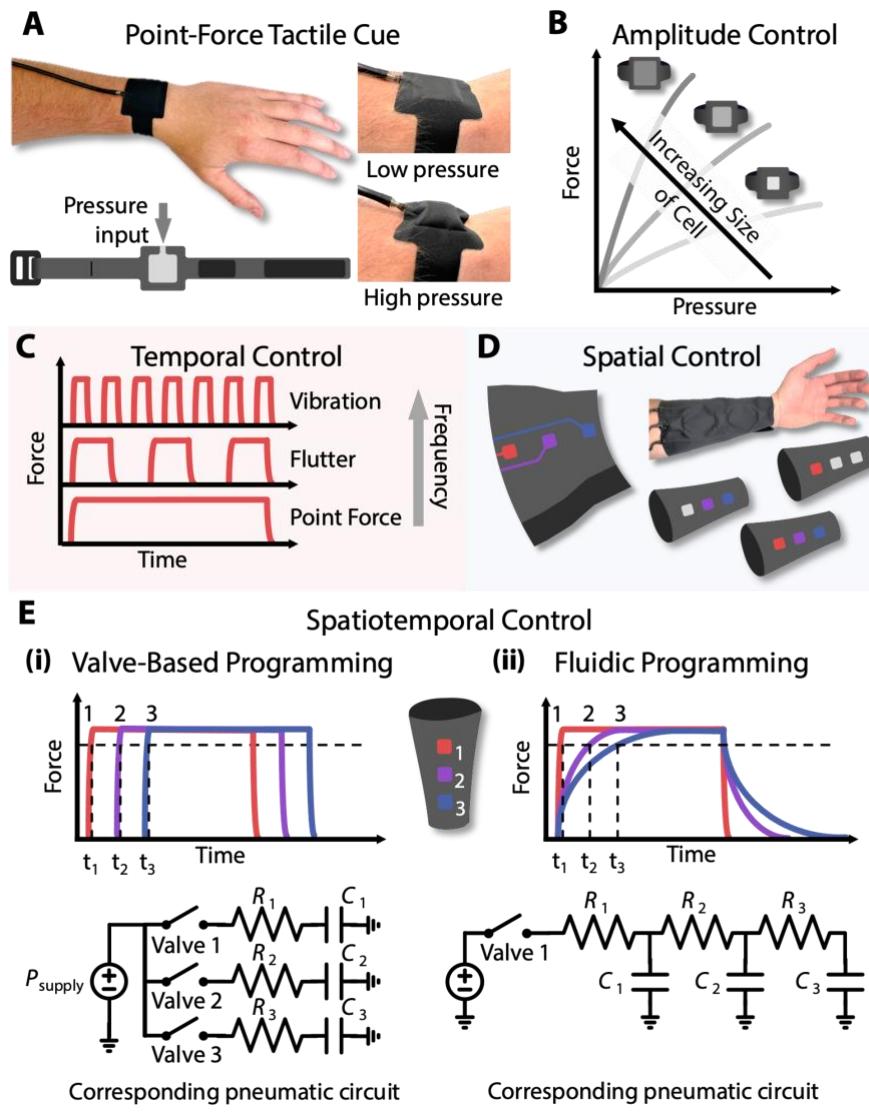
Figure 1. Schematized concept of wearable haptic textiles. (**A**) The pressure-driven expansion of a textile cell imbues a point-force tactile cue when constrained by a band wrapped around the wrist. (**B**) The applied force is controlled by regulating the internal pressure, and the relationship of force to pressure can be engineered based on the internal geometry. Temporal control (**C**) enables cues ranging from a constant point force to rapid succession of momentarily applied forces to achieve flutter and emulate vibration. Spatial control (**D**) is enabled by integrating multiple cells at a distance beyond the two-point discrimination threshold. Both temporal and spatial control can be combined for spatiotemporal control (**E**) to provide higher-dimensional cues and unique sensations, either through external programming of individually addressable valves (**E-i**) or through embedded fluidic programming based on engineered internal fluidic resistances and capacitances (**E-ii**), reducing the requirements for external infrastructure.

We characterized our single-cell wristbands by varying the equal-length sides of the rectangular geometry across four values: 15, 20, 25, and 30 mm (Figure 2A). The cells output a force normal to the surface of the skin; we recorded this force in an instrumented test rig (Figure S3) that emulates the anatomical dimensions and elastic modulus of a human wrist.[27] Beyond the effect of preload (Figure S4), the force of a single-cell wristband depends on both the supplied fluidic pressure and the areal geometry (characterized by the length of one side of the square region). Both parameters can be tuned or designed based on the target application. We show that our single-cell wristbands exhibit amplitude control across two "dimensions" (i.e., both geometrically and fluidically) in Figure 2B.

A pneumatic pressure source inflated each cell from 0 to 1 bar at increments of 0.1 bar. This pressure range is typical for soft robotic devices and is achievable by compressors and other sources of pressurized air,[83] including a wearable pneumatic energy harvesting system.[84] Examining the effects of the internal geometry of the cell across three trials (Figure 2B), the steady-state force at a given pressure correlated positively with the characteristic length; that is, the largest cell (30 mm in width) demonstrated the largest forces (0–19 N), whereas the smallest cell (15 mm in width) produced the smallest forces (0–0.65 N). Each of the geometries exhibited functionally similar monotonic responses of force with respect to pressure. We recorded the transient force responses; the cells pressurize at a rate that follows the input step function closely (Figure S5).

We also investigated the bandwidth of our single-cell wristbands, which is particularly important in haptics (e.g., in vibration). Previous research has demonstrated that point-force cues begin to feel like "flutter" when provided at frequencies on the order of 10 Hz, and flutter begins to feel like vibration when cues are delivered on the order of 100 Hz.[85] We characterized our single-cell wristbands in terms of their attenuation of pressure (dB) as a function of frequency (Figure 2C). Using a high-frequency solenoid, we periodically actuated each of the wristbands in the same fashion as the static testing. Increasing in frequency (1–60 Hz), we measured attenuation relative to the static steady-state force observed in Figure 2B. We define our cutoff frequency (i.e., the baseband bandwidth) at -3 dB. All four cells surpass 10 Hz (Figure 2C) and can thus provide both point-force cues and flutter cues but did not achieve vibration, nevertheless surpassing the frequency of other haptic devices that claim vibration (table S1). Notably, the size of the cell adversely affects the magnitude of attenuation for a given frequency due to the increased volume

(i.e., fluidic capacitance); the smallest and largest cells had a bandwidth of 15 Hz and 12 Hz, respectively. More information regarding the volume of a cell is provided in the Supplemental Text (Equations S1– S2) and in Figures S6–S9. Furthermore, although the solenoid was rated for more than 1,000 Hz, we observed that a "zero-volume" setup exhibited a similar bandwidth (20 Hz) to the setup that incorporated our cells with their constituent added volumes (inset, Figure 2C), due to the conflated limitations imposed by the upstream fluidic and electromechanical subsystems.

Finally, we characterized the variation of force outputs for single-cell wristbands due to experimental error or inconsistencies in fabrication (Figure 2D). We show the steady-state force response for three separately manufactured wristbands with a characteristic length of 30 mm, chosen for the largest range of forces that represent the upper limit of expected tolerances in nominal values of force; each wristband was tested three times, resulting in 9 trials per interval of pressure. The average difference in force between the trials is 16%, indicating sufficient reliability in our experimental and manufacturing methods.

We note that the 25-mm cell exerts an output force of 0–9.8 N across input pressures of 0–1 bar, mirroring the desired range of 0–10 N for tactile cues.[27] Furthermore, the difference in attenuation of force under time-varying pressure signals due to added fluidic capacitance compared to the other sizes of cells (and the zero-volume case) is negligible, and the outward expansion from the wrist is 6 mm measured orthogonally, generating an unobtrusive profile. Due to these considerations, for the remainder of this work, our devices use 25-mm by 25-mm cells.

Spatiotemporal Control through Valve-Based Programming
We expanded our device from a single-cell wristband to a multi-cell sleeve, made from the same materials and two-layer stacked-lamination method (Figure S2). As shown in Figure 3A, the sleeve contains three 25-mm cells oriented along the proximal-distal axis, located on the ventral side of the forearm (where the skin is more glabrous, i.e., less hairy, and thus more sensitive to tactile cues). Furthermore, the use of the forearm is beneficial over alternative body parts because of its available surface area relative to its density of mechanoreceptors while not occluding real-world sensations through one's hands and fingers.[86] The equal spacing between the cells places them beyond the forearm's threshold for two-point discrimination at a cell-to-cell distance of 45 mm.[87] Similar to the single-cell wristbands, the multi-cell sleeve is secured to the arm with hook-and-loop fasteners on opposing edges.
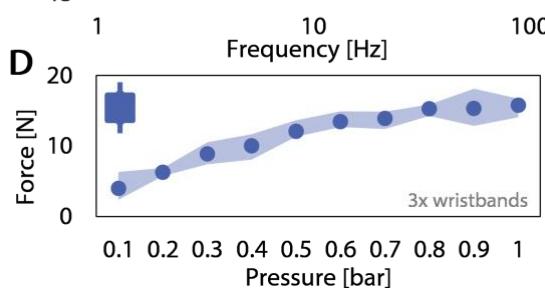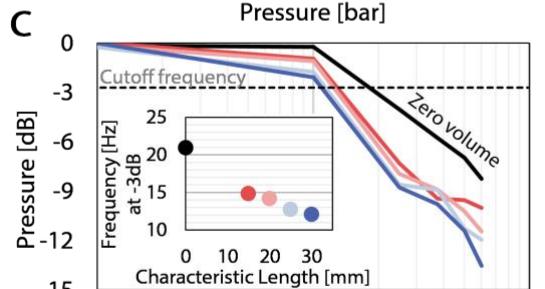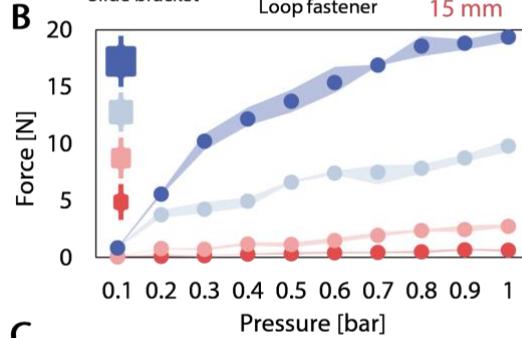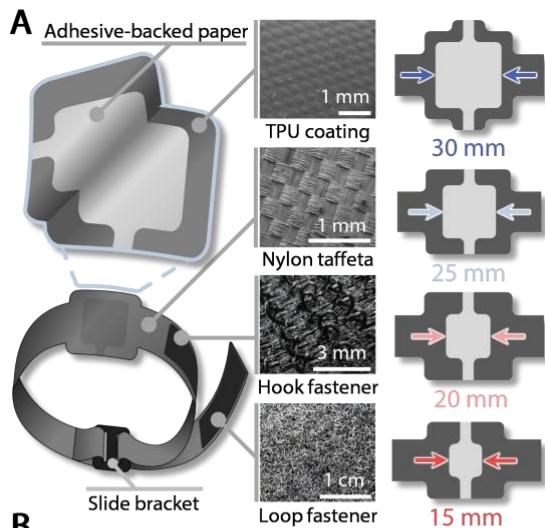
Figure 2. Characterization of a single-cell haptic textile wristband. (**A**) Wristband with an inflatable cell made from TPU-coated nylon taffeta with adhesive-backed paper defining the internal geometry. The wristband is secured by hook-and-loop fasteners and made easily adjustable by adding a slide bracket. Four sizes of internal geometries were tested: 30, 25, 20, and 15 mm. (**B**) The four wristbands had positively correlated force responses to input pressure and the characteristic length of each cell. Error (shaded region) represents minimum and maximum steady-state forces of three trials. (**C**) Dynamic characterization of the wristbands revealed that their bandwidths trend with the size of the cell yet exhibit similar bandwidths to the controller with no wristband attached, i.e., zero volume. (**D**) Three 30-mm wristbands were tested to examine combined variability from experimental procedure and manufacturing. Error (shaded region) represents minimum and maximum steady-state forces from the averaged trials of each of the three bands.

Based on our results in Figure 2C, the differing lengths of channels leading to the cells are approximately equal and negligible in their resistance relative to the resistance that the overall fluidic-electromechanical system introduces (Figure 3B). We allocated one solenoid valve per cell, allowing for individually addressable, spatially discriminable point-force cues. The solenoids control whether the cell is unpressurized (denoted as a binary "0") or pressurized (binary "1").
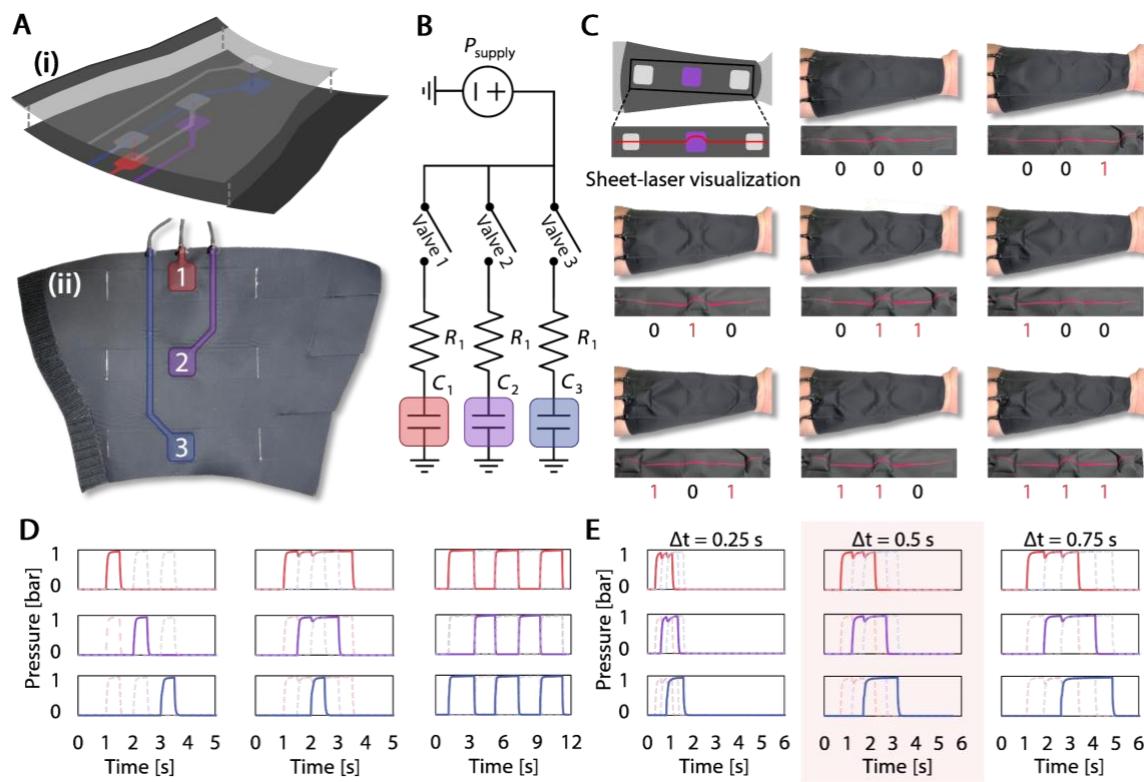

Figure 3. Characterization of a multi-cell haptic textile sleeve. (**A**) The multi-cell sleeve contains three internal 25-mm cells spaced axially along the forearm, shown as a schematic (**i**) and a false-colored photograph (**ii**). (**B**) The corresponding pneumatic circuit of our multi-cell sleeve depicts a pressure source, P_{supply}, that is gated by one solenoid valve (fluidic switch) per cell (fluidic capacitor). The resistance of the internal channels between the cells and electromechanical system are shown equal to each other here, but are negligible compared to the resistance imposed by the system upstream of our textile device. (**C**) Three cells allow for three fluidic bits and eight binary states to be encoded with external control. (**D**) The eight binary states can be further expanded by incorporating temporal variation to provide a vast array of spatiotemporal cues. (**E**) Various durations of spatiotemporal cues were pilot tested to find a salient illusory stroking motion delivered by the cells sequentially inflating, leading to the selection of a 0.5-s delay between each cue for our simplified control scheme through material-based fluidic programming.

The three fluidic bits facilitated by the three cells allow for eight (2^3) binary states to be realized (Figure 3C). The binary states enable a direct way to communicate information to the user when trained on the meaning of each of the eight states. The user can passively feel the cells and discern which bits are "high" and which are "low" without having to directly interact with the sleeve, although complementary active exploration of the cells (by touching directly with one's fingers) is feasible. Moreover, the inflated regions can provide additional visual feedback as well, thus yielding multisensory feedback (passive and active haptic cues in combination with visual cues).

Beyond the static binary states, we employed valve-based timing for spatiotemporal control. Spatiotemporal cues enable communication at a higher resolution than one-dimensional (temporally or spatially variant) cues by allowing each combination of positioning and timing to have a defined meaning or intent. Figure 3D demonstrates three combinations of cues. The first demonstration consists of a simple sequential on-off scheme for the cells, progressing distally along the forearm. The second shows an on-on-on-off-off-off combination where the cells progressively pressurize distally and then depressurize proximally. The last demonstrated combination pressurizes the most proximal and distal cells at the same time and then flips their coupled states to the opposite state of the middle cell.

We also investigated cues that progress along the arm, emulating a stroking motion, of which there has been interest for social and therapeutic applications.[50,51,53,88] We pilot tested multiple temporal combinations in which each cell was sequentially pressurized until all were inflated, after which the cells were depressurized in the same order, creating a tactile illusion of stroking. We show the three differential times between cues that felt the most salient and realistic to the authors (0.25 s, 0.5 s, and 0.75 s) in Figure 3E, and provide other durations in Movie S1. Of these, we found a temporal spacing of 0.5 s provided the most salient illusory stroking motion. Nevertheless, we note that many combinations of spatial and temporal inputs could be created with valve-based spatiotemporal control, allowing for a wide array of cues that are highly tunable to meet various constraints or preferences, perhaps including alternative tactile illusions such as the cutaneous rabbit illusion, the kappa effect, the tau effect, and others.[89–91] As for the decision to use three cells, the incorporation of more than two cells enhances the effect of continuous motion,[50] whereas four or more 25-mm cells (and their associated channels and resistors) would be too large for the forearm of a typical user.

Increasing the number of combinatorial inputs ultimately comes at the cost of portability. Valve-based spatiotemporal control requires one solenoid valve and one pneumatic input per cell (i.e., per fluidic bit), a multi-channel controller to regulate the valves and pressure source(s), and components to power the electronics and to accumulate (and pressurize) the working fluid. Consequently, the overall system quickly outgrows its original low-profile and lightweight design, evolving into a bulky entanglement of hardware. This approach has merit in stationary environments for work or entertainment, including remote navigation, telesurgery, gaming, and other media.[92–97] Yet, for more portable and unobtrusive wearable haptics, a simplified control scheme is necessary to circumvent the drawbacks of electromechanical systems that individually address each cell for spatiotemporal cues.

Material-Based Fluidic Programming of Spatiotemporal Cues
We introduce a simplified control scheme in our wearable haptic textiles through embedded fluidic programming. We built fluidic circuits composed of analogs to resistors and capacitors to facilitate spatiotemporal cues in lieu of bulkier and more expensive solenoid valves. Iterating from our multi-cell sleeve, we designed a programmed fluidic circuit integrated into a textile module (Figure 4A) that contains three 25-mm cells capable of delivering up to 10 N of force, each of which acts as a fluidic capacitor. The added fluidic resistors composed of soft open-cell foam fit compactly within footprint of the multi-cell sleeve, and this device uses three (rather than two) layers of HST and fluidic "vias," borrowing a concept from electronic printed circuit boards.[68]

The device sequentially pressurizes (and similarly depressurizes) the three spatially discernable cells at times governed by the fluidic resistors integrated between each of the connected cells; in essence, the device acts as a compound resistor-capacitor (RC) circuit for N capacitors (cells) and N-1 resistors (neglecting R_1, the upstream resistance due to the internal channels). The pneumatic circuit in Figure 4B illustrates how the resistance (R_2) between Cell 1 (with capacitance C_1) and Cell 2 (with capacitance C_2) causes a delayed rate of pressurization of C_2. Prior to Cell 3 (with capacitance C_3), a resistance (R_3) 3x that of R_2 introduces a further delay in pressurization between cells C_2 and C_3. The resistances allow for a single input to trigger a spatiotemporal cue, whereas the previous valve-controlled multi-cell sleeve requires one input per cell (i.e., three inputs for this design reduced to one).
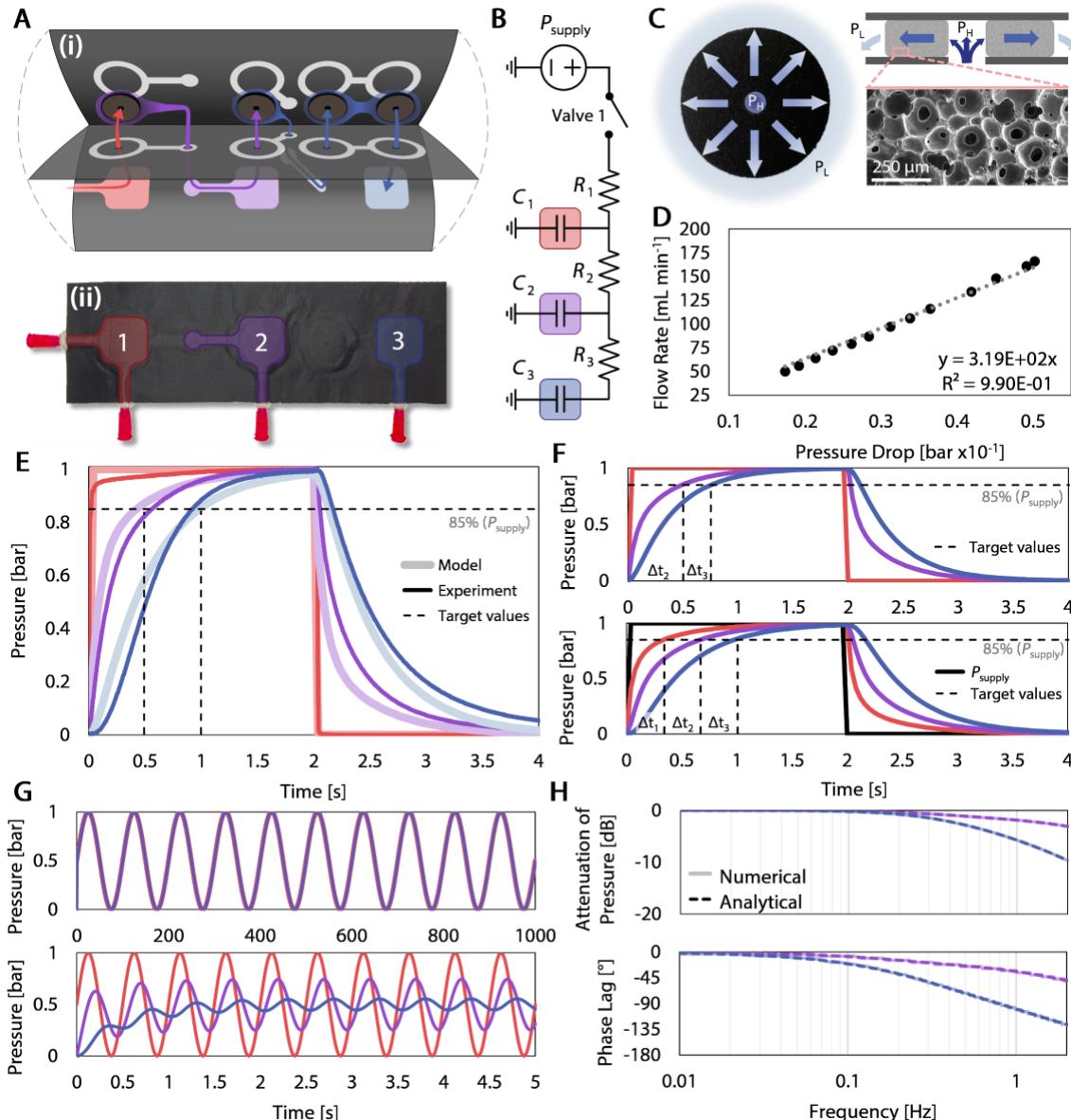
Figure 4. Fluidically programmed haptic textile module. (**A**) Three 25-mm cells were spaced equally with foam resistors between each cell (**i**). A false-colored photograph shows the module with pressure-sensing ports added at each cell for data collection (**ii**). (**B**) The corresponding pneumatic circuit depicts the resistor-capacitor (RC) circuit for the programmed textile module. (**C**) An annular open-cell foam resistor impedes flow in the radial direction due to its microporous structure. (**D**) Flow rate versus pressure drop for an annular foam resistor of 22-mm outer diameter and 3-mm inner diameter. (**E**) Numerical model of each cell's pressurization compared to experimental data. (**F**) Alternative programming demonstrates the utility of the numerical model in designing spatiotemporal cues. Top: 22-mm by 3-mm and 24-mm by 1-mm resistors for R_2 and R_3, respectively, provide a 0.5-s delay (Δt_2) before C_2 reaches its target pressure, followed by a 0.25-s delay (Δt_3) for C_3. Bottom: Adding a resistor upstream of C_1 allows for the cell to pressurize after the input goes high (Δt_1), while maintaining equal temporal distance between cues ($\Delta t_1 = \Delta t_2 = \Delta t_3$). (**G**) Time-variant (sinusoidal) inputs for 0.01 Hz and 2 Hz are numerically solved. (**H**) Attenuation of pressure and phase lag for the sinusoidal input waveform (swept across 0.01–2 Hz at 0.01-Hz intervals) are calculated from the numerical solution and analytically derived, showing good agreement between approaches.

The fluidic resistors (Figure 4C) are fabricated from 1.6-mm-thick open-cell polyurethane foam that is permeable but considerably impedes airflow. The fluidic resistance of each annular foam resistor is 3.19×10^3 mL min^{-1} bar^{-1} (Figure 4D). The foam is mechanically and fluidically robust, yet soft and compliant while retaining a low profile, making it well-suited for integration into two-dimensional, textile-based devices.[68] The resistors are thermally bonded between layers of HST, preventing fluid from flowing through the top or bottom surfaces. The fluid may then only flow through the center hole and outward radially through the porous foam until reaching the outer radius, shown in Figure 4C. Conversely, the fluid may flow inward radially if the pressure is higher outside the annulus relative to its center.

Following Darcy's law for flow through a porous medium, the annular geometry of the resistor facilitates a logarithmic relationship with pressure drop (Equation S3), minimizing sensitivity to small errors in geometry due to fabrication. The resistance depends on the inner and outer radii of the annular resistor and the fluidic sheet resistance (analogous to electrical sheet resistance). The fluidic sheet resistance is a function of the thickness and permeability of the sheet and the viscosity and density of the working fluid; in this case, we measured the overall fluidic resistance of our annular foam resistor with outer and inner diameters of 22 mm and 3 mm, respectively, by fitting a line to the pressure drop across the resistor as a function of flow rate (Figure 4D), residing within 4% of the expected analytical value (see Supplemental Text).

In order to program the fluidic control of our spatiotemporal device, we developed a numerical model that—for any arbitrary input pressure—iteratively solves for the mass flow rate between two adjacent cells as a function of the differences in pressures and the linear (i.e., Ohmic) fluidic resistance between the cells (Equation 1). The ideal gas law dictates the relationship between pressure (P), volume ($\mathcal{V}$) (shown in figs S6–S9 and empirically derived in the Supplemental Text), and mass (m) for a given temperature (T_g) and specific gas constant (R_g). By conservation of mass, Equation 2 provides the first time derivative of P. For a system of four cells, which we implement for later use in simulating upstream resistance of the first cell, we show in Equation 3 the matrix form of the solution derived from Equations 1 and 2.

$$\dot{m}_{i-1\rightarrow i}=\frac{\left(P_{i-1}-P_i\right)}{R_{i-1}}\tag{1}$$

$$\frac{d}{dt}P_i=\frac{R_gT_g}{V_i}\left(\dot{m}_{i-1\rightarrow i}-\dot{m}_{i\rightarrow i+1}\right)\tag{2}$$

$$\frac{d}{dt}\begin{bmatrix}P_2\\P_3\\P_4\end{bmatrix}=\begin{vmatrix}-\frac{1}{V_2}\left(\frac{1}{R_1}+\frac{1}{R_2}\right)&\frac{1}{V_2}\frac{1}{R_2}&0\\\frac{1}{V_3}\frac{1}{R_2}&-\frac{1}{V_3}\left(\frac{1}{R_2}+\frac{1}{R_3}\right)&\frac{1}{V_3}\frac{1}{R_3}\\0&\frac{1}{V_4}\frac{1}{R_3}&-\frac{1}{V_4}\frac{1}{R_3}\end{vmatrix}\begin{bmatrix}P_2\\P_3\\P_4\end{bmatrix}+\begin{bmatrix}\frac{P_1(t)}{V_2R_1}\\0\\0\end{bmatrix}\tag{3}$$

Based on our numerical model, we predicted that a set of four annular resistors with outer and inner diameters of 22 mm and 3 mm, respectively, could create the desired 0.5-s temporal delay between cues (Figure 4C). We placed one resistor between cells C_1 and C_2 and placed three resistors in series between cells C_2 and C_3. The resulting experimental data in Figure 4E align well with our model, showcasing the ability to predict and ultimately design spatiotemporal responses based on parameters of the fluidic system.

To demonstrate the predictive utility of our fluidic model, we show in Figure 4F two alternative sets of programmable cues that could be implemented in a similar device. The top programmed response is based on the same annular resistor for the resistance R_2 (before C_2) but has a resistance R_3 that is 1.6 times the resistance of R_2 (which could, for instance, be obtained with an annular resistor that has a 24-mm outer diameter and a 1-mm inner diameter). The resulting cue creates a 0.5-s delay between the first two cells (C_1 and C_2) but only a 0.25-s delay between the last two cells (C_2 and C_3). The other programmed response implements a resistance upstream of C_1 (using the four-cell solution in Equation 3). In this way, the supplied pressure does not instantaneously inflate C_1, but delays it by 0.33 s. The following cells are also delayed by 0.33 s from their predecessors. This programming occurs with respective normalized resistances of [0.5, 0.7, 1.9] for R_1, R_2, and R_3, where the resistance of a 22-mm by 3-mm annulus represents unity.

We further expand our model to predicting the attenuation of pressure and phase lag of periodic functions, which are analytically tractable (compared to the time-stepping solution required for an arbitrary input). Using an alternating current (AC) analysis of a

parallel RC circuit, we derive the steady-state response of our device to sinusoidal inputs, yielding predictions for the attenuation and phase lag (Figure 4G, Equations S5–S9).

Using the numerical model, we conduct a frequency sweep from 0.01 Hz to 2 Hz at 0.01-Hz intervals (Figure 4G), noting that sinusoidal frequencies above 2 Hz cause attenuation of the pressure in downstream cells beyond -3 dB. Comparing the analytical solution to the numerical simulation, Bode plots in Figure 4H report the attenuation and phase lag across the range of frequencies. Our numerical model again aligns well, this time with the analytical solution, indicating the robustness of the two methods for predicting and designing spatiotemporal cues. Additionally, we present square, triangle, and sawtooth waveforms in Figures S10–S12 to show the pressure responses of each cell for alternative periodic functions. The variety of periodic waveforms and the ability to analytically understand them reveal the potential for control schemes that tune amplitudes (attenuation) and temporal delays (phase lag) across spatial dimensions, further expanding the capabilities of our haptic textiles to entirely new paradigms of cues not yet explored in fluidic haptics.

Our numerical model, analytical model, and experimental data demonstrate that we can dependably program spatiotemporal cues into the constituent material of the haptic textile through the incorporation of fluidic RC analogs. As a result, the reliance on bulky infrastructure for delivering spatiotemporal cues is substantially reduced relative to valve-based programming; our fluidically programmed module provides a multidimensional cue with a single input (of constant or periodic pressure). To determine the haptic efficacy of our wearable haptic textiles with material-based fluidic programming, we tested the haptic textiles on human participants by combining the spatiotemporal cues from the described simplified control scheme into more complex directional cues.

Haptic Efficacy of Textile-Embedded Fluidic Programming
We implemented two fluidically programmed textile modules in opposing orientations into the same footprint as the multi-cell sleeve (Figure 5A). In this configuration, the sleeve can provide spatiotemporal cues (with a differential time between cells of 0.5 s) in the proximal and distal directions, using a single constant-pressure on-off input (i.e., one solenoid valve) for each spatiotemporal cue. We separated the two sets of cells in the transverse direction by 20 mm, which is less than the forearm's threshold for two-point discrimination.[87] Two sleeves fabricated in this manner—one for the left arm and one for

the right arm—ultimately require 4 inputs rather than the 12 inputs that would be required to deliver the same cues with valve-based programming, reducing the requirement for valves by 67%.

We indicated four directions from two sets of two spatiotemporal cues (i.e., the four input lines attached to the two sleeves, Figure 5B). Forward directions were indicated by the left and right arms having distally propagating cells; backward directions were indicated similarly, but in the proximal direction. Left and right directions had both the distally and proximally propagating cells actuate on the sleeve worn by the corresponding arm.

We conducted a human-subject experiment with 14 participants (6 female, 12 right-handed, aged 20–27 years, with an average age of 23 years). As shown in Figure 5C, an opaque sheet covered the participants' arms to prevent any visual indication of the delivered cue, and headphones covering their ears played pink noise to prevent any auditory feedback that could assist the participants in determining the delivered cue. The participants overall scored an average accuracy of 87.3% (Figure 5D); however, the responses were generally split across two groups (Figures S13–S14). Excluding the non-responders and looking at the accuracy for the participants above the median, the adjusted average accuracy in Figure 5D jumps to 97%. We also show the participants' cumulative responses in a "ladder plot" in Figure 5E, where the lines are directed from the input to the response and the weight of each line indicates the magnitude of that response. Generally, the erroneous responses are systematic, particularly regarding the forward and backward directions being the most frequently confused cues with a combined error of 7.1%. Nevertheless, these results indicate that fluidically programmed wearable haptic textiles offer a satisfactory efficacy in delivering spatiotemporal cues. Combined with the system's reduced encumbrance, textile-embedded spatiotemporal cues can be reliably tested and implemented in more realistic scenarios beyond the laboratory.
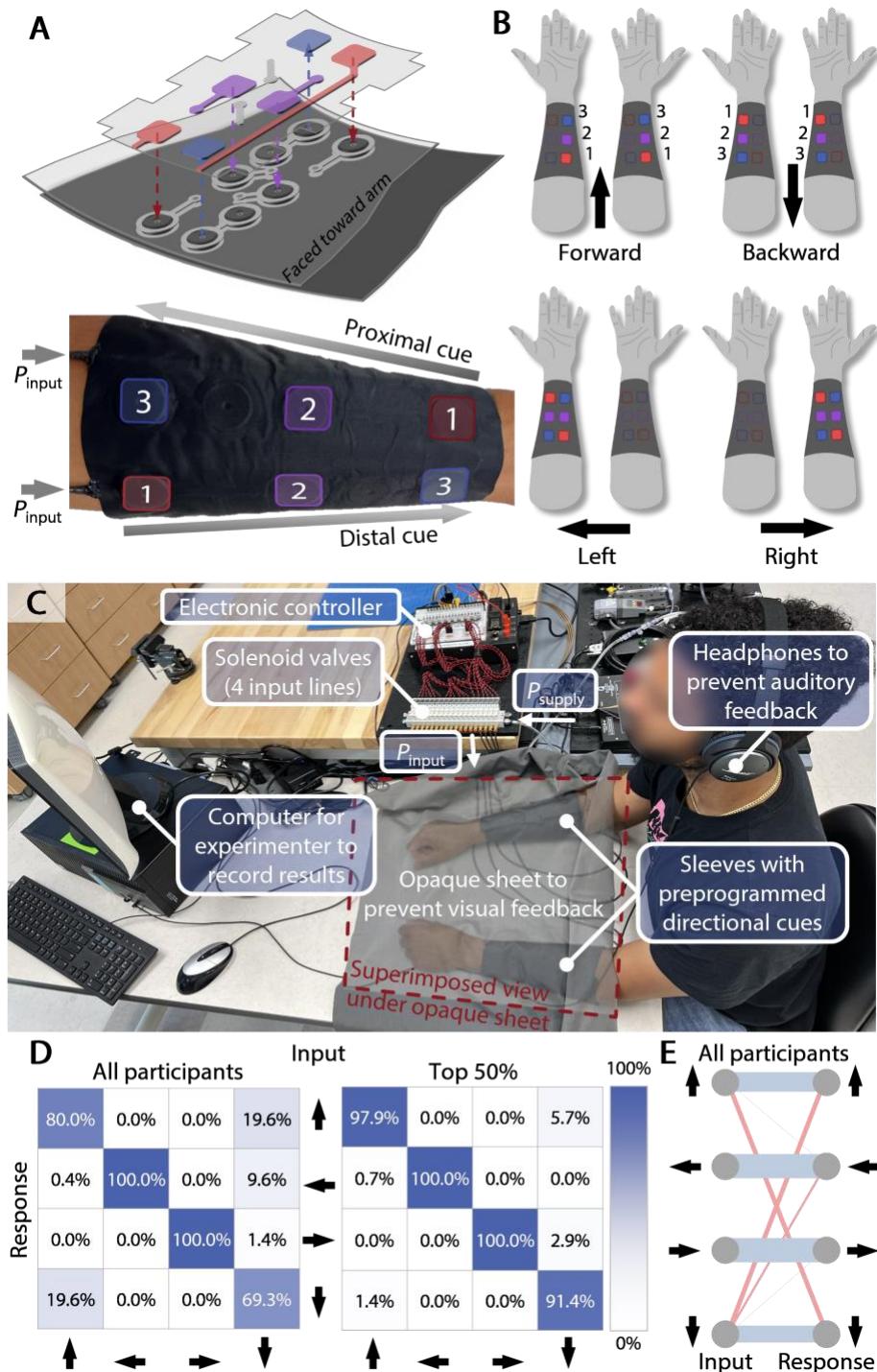
Figure 5. Haptic cues from fluidic programming. (**A**) Two sets of three cells each, programmed to deliver spatiotemporal cues in opposite directions, were integrated into a sleeve for the forearm. (**B**) Four spatiotemporal cues from two sleeves, with each cue actuated by one pressure input. (**C**) A participant receives cues for four different directions and relays the perceived cues to the experimenter. An opaque sheet covered the participant's arms during testing to prevent visual feedback; here, we show a superimposed image of their arms for viewing purposes. (**D**) Results from human subjects showing the accuracy of the fluidically programmed directional cues for all participants (left) and the top half of participants (right). (**E**) Ladder plot with line weights between inputs and responses corresponding to the proportion of participants' responses, where the blue lines are correct responses and the red lines are incorrect responses.

Fluidic Haptic Textiles Beyond the Laboratory

Because the fluidically programmed functionalities are well-suited for tasks that require delivery of repeated sets of information, such as navigation, teleoperation, and notifications, we opted to implement our haptic textiles into a wearable format for directing a user in navigation. We integrated two sleeves identical to those designed for the human-subject experiment into a shirt (Figure 6A) and procured an elastic textile belt to which auxiliary components were attached with hook-and-loop fasteners (Figure 6B). Four tubes routed through the shirt connected the pneumatic inputs to miniature solenoid valves soldered to a belt-mounted circuit board powered by a 9-V battery. A 4-channel wireless remote sent 433-MHz signals corresponding to the four directions that were delivered to the user by the portable supply of CO_2 (Figure S15). The controller could run continuously for over 40 hours while providing one cue per minute based on the current draw of the components and the capacity of the battery. With these systematic upgrades and reduced reliance on solenoid valves, our haptic textiles are capable of communicating to a user in real-world scenarios without being constrained to a benchtop setting.

A user donned the untethered portable device, and the experimenter provided haptic cues to direct the user in waypoint-based navigation for walking 1 km in one test and operating a scooter for 1 km in another test (Figure 6C, Figure S16, and Movie S2). The user accurately followed the target routes as indicated by the data from the global positioning system (GPS) receiver installed on the user's mobile phone (Figure 6C). We indicated the haptic cues through the wireless remote from afar, and the user was unaware of the intended route or destination in any of the untethered tests. The user interpreted the cues with 100% accuracy, even while operating the electric scooter over vibration-inducing paved bricks, concrete sidewalks, and graveled paths. Our spatiotemporal force cues are thus well-suited for untethered navigation, as the vibrations felt from the travel could cause issues with the more typical vibrotactile signals seen in commercial wearable haptic devices due to neural adaptation leading to vibrotactile desensitization.[98]

We wirelessly directed the same user to draw various "one-sided" (i.e., chiral) tetrominoes in an open field (Figure 6D, Figure S17, and Movie S3), where four unit squares are orthogonally connected to form a shape that is distinct when reflected. These tetrominoes represent the 90-degree corners present in typical navigational instructions in the real world yet allow for a more difficult mode of unstructured testing without preexisting surface streets for reference and, consequently, demonstrate applicability beyond the

specific use case of navigation alone. Figures 6E through 6G show the tetrominoes with reflectional symmetry and the GPS data of the user's path. Figures 6H through 6K show the chiral pairs of the remaining two tetrominoes. As in the waypoint-based tests, the user responded to each cue with 100% accuracy for walking each shape in an open field, where left, right, and forward cues indicate directionality and a single backward cue indicated stopping or "arriving at destination." We also directed the user to draw two Π symbols, where a reversal (indicated by two backward cues in rapid succession) was required for the non-polyomino form (Figure S18, Movie S3).

Although textile devices in our prior work have been shown to operate for more than 20,000 cycles of actuation and over a million flexions,[68] our final two tests examined the mechanical robustness of our fluidic haptic textiles by subjecting the fluidically programmed module to potential scenarios found in real-world use. The first test of robustness included washing our programmed textile module 25 times in a washing machine (Figure 6L). After each set of 5 washes and allowing the module to dry, we tested the pressure response of the cells. The 5 sets of data, compared against pre-washing data, indicate that the module is largely unaffected by washing. For the same module that was washed, we then punctured cell C_2 with a knife such that the device was unable to provide spatiotemporal pressure responses. We repaired the module by thermally bonding a patch of HST, 20 mm in diameter, with a household iron (Figure 6M, Movie S4). Figure 6N shows the data for the short-circuited module, where cells C_2 and C_3 exhibit negligible pressures and thus a failed spatiotemporal cue. After the repair, the module resumed normal operation and was fully functional. These two tests demonstrate that our devices are robust, yet even in the event of a catastrophic failure, the functionality remains the same after patching with a common household appliance.

Discussion

Borrowing concepts from fluid mechanics and material intelligence, this work presents a platform for embedding fluidic analog control directly into wearable textiles. To illustrate the broad potential of our fluidically programmed haptic textiles,[99] we explored the combinatorial aspects of simplified control schemes (through fluidic haptic circuits programmed into the device), multi-modal cues (through hierarchical temporal and spatial control), and elementary methods of actuation (based on the tailorable forces induced by the inflation of a cell). We achieved these capabilities through a process of fabrication that is more consistent and amenable to automation relative to the existing literature for soft

(and particularly soft haptic) devices. The outlined steps for fabrication (Supplemental Information and Figure S2) require minimal training to follow and provide the means to create advanced wearable systems at a low cost (regarding materials, tools, and time). For reference, the single-cell wristband costs less than $1 in materials, and the fluidically programmed sleeve costs less than $4. Accordingly, our methods detail a process that lends itself well to low-resource settings, lowering barriers to entry, and yet is capable of creating useful, low-profile technology. Our manufacturing techniques are derived from the apparel and textile industries, in which stacked-sheet lamination is a common technique to fabricate clothing and other textile-based products that interface with humans. This approach to fabrication can be scaled up to enable high-throughput and economical manufacturing as has already been done for other heat-sealable textile products, such as gear and equipment in the recreational, medical, and military industries. There has also been a recent push to reduce waste in the textile industry,[100] and accordingly the materials we use are thermally, chemically, or mechanically recyclable.[101] Furthermore, textile-based devices can be easily repaired (rather than discarded) by heat-sealing patches over any tears or leaks (Figures 6M–N and Movie S4). In short, our methods and materials for fabrication enable a circular and sustainable process.

While we demonstrate a diverse set of tactile cues in this work (such as combinatorial inputs in the multi-cell sleeve and time-variant inputs in the programmable textile module), the introduction of material-based fluidic programming to haptics enables an even broader array of potential wearable haptic devices beyond those we have shown here. For instance, harnessing mechanofluidic instabilities could provide higher frequency actuation to circumvent the encumbrance of electromechanical valves altogether and their limited bandwidths.[63,102] In another potential future direction, a wearable haptic device capable of multisensory cues (passive, active, visual, and others) could be created from inflatable textiles.[28,33,47] Alternatively, researchers could investigate the relevant psychophysics behind the new paradigms of cues resulting from the ramped RC-response of force, compliant pressure-based actuation, or the salience of cues integrated into more loosely fitting clothing. A theoretical approach to the geometric dependence of the force profiles could also be investigated.

Regarding the devices shown here, we provide an in-depth characterization of our wearable haptic textiles and demonstrate their ability to provide point-force cues with programmable amplitude, spatial, and temporal control. The amplitudes of force are

controllable by pressure-based or geometric means, while the spatially discriminant cells can be tailored to cover short or long distances across a portion (or the entirety) of the body. We demonstrated spatiotemporal delivery of cues through typical valve-based methods as well as through fluidically programmed control enabled by the intrinsic material properties of open-cell foam fluidic resistors. The material programming of our fluidic system simplifies the control scheme and negates the need for extraneous solenoid valves beyond the single valve needed to initiate each spatiotemporal cue; here, we reduce the required valves by 67% (from 12 to 4), but the fluidic programming approach can also lend itself to reduce hardware by a greater factor depending on the complexity of cue. The sophisticated cues enabled by our textile-embedded fluidic programming were further tested in a human-subject experiment across 14 participants and were demonstrated to be effective "in the wild" for navigating city streets and drawing tetrominoes with GPS data. The accuracy of information transfer via the fluidically programmed sleeves proved the haptic efficacy across multiple people for providing four directional indicators, and the untethered demonstrations showed that our device can be implemented in real-world settings by being portable and integrating seamlessly into existing garments, in contrast with many state-of-the-art haptic devices. Ultimately, this approach to fluidically programming haptic textiles represents an integral step toward active clothing that can assist or enhance our day-to-day interactions.
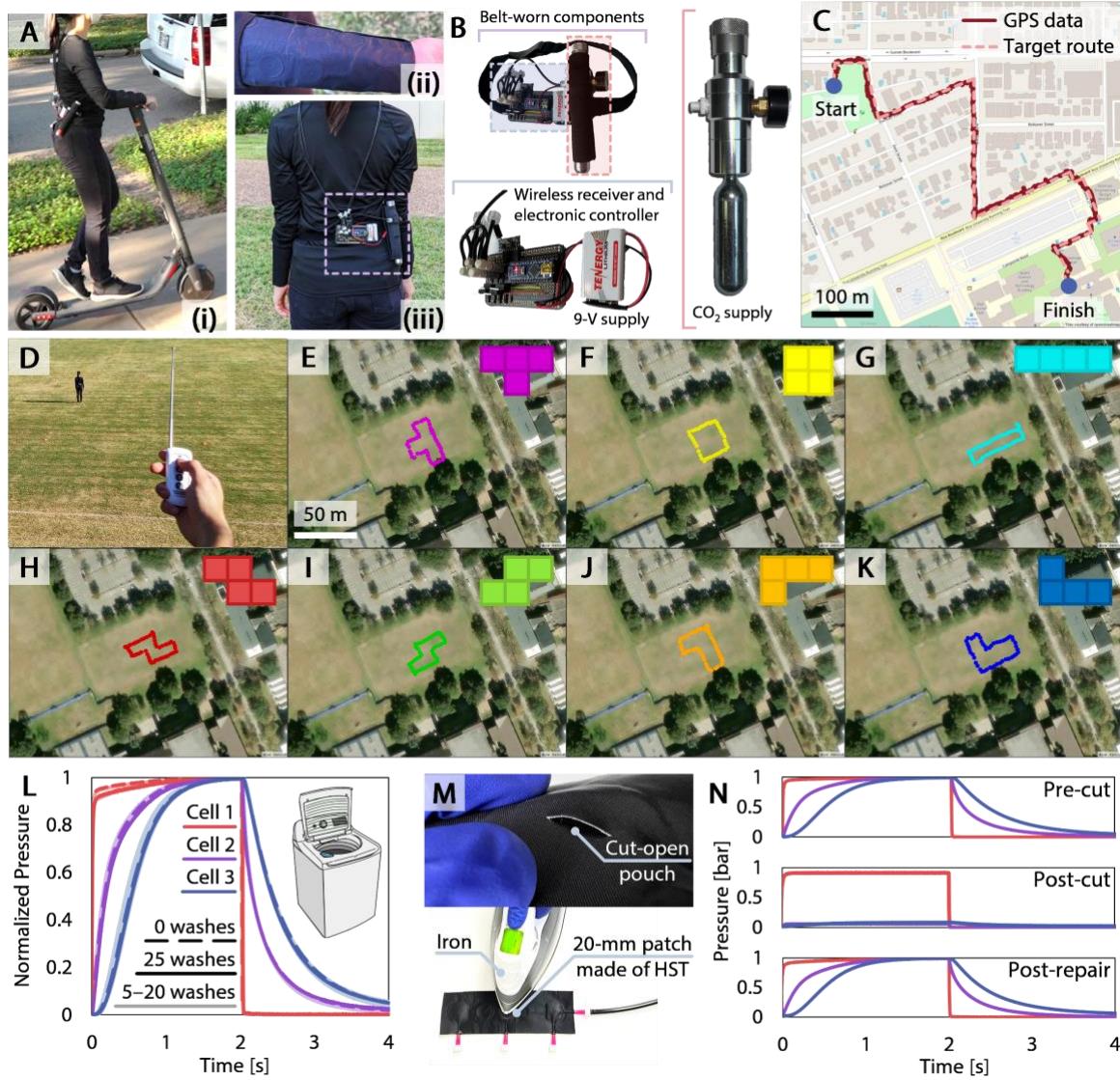
Figure 6. Real-world demonstrations of fluidically programmed wearable haptic textiles. (**A**) A user navigates on a scooter (**i**) with the fluidically programmed sleeves integrated into a shirt (**ii**) and controlled by a circuit board and powered by a canister filled with compressed gas worn on the belt (**iii**). (**B**) The circuit board contains only four miniature solenoids (as opposed to the 12 solenoids that would be required by a comparable system without fluidic programming), as well as a wireless 4-channel receiver and a microcontroller, powered by a 9-V battery and used to gate the flow from the pressurized CO_2 canister. (**C**) With this portable system, the untethered user was wirelessly directed to multiple waypoints over 2 km, including walking (Figure S16) and operating a scooter. (**D**) The user was also directed from a tower overlooking an open field to "draw" tetrominoes by walking. (**E–K**) The GPS data of the 7 tetrominoes drawn by the participant. (**L**) After 25 washes, the device remains fully functional; pressure data recorded after every 5 washes. (**M**) The second cell was cut open by a knife and then repaired by ironing a patch of HST over the cut. (**N**) The module exhibited short-circuited pressure responses after the cut but resumed normal operation after repair.

Experimental Procedures

Characterization of Single-Cell Wristbands

The single-cell wristbands (Figure 2A) were strapped around an instrumented emulative wrist rig (Figure S3) and were tightened to a 1-N preload. The wristbands were inflated at 0.1-bar increments from 0 to 1 bar of pressure, verified by pressure sensors (ADP5151, Panasonic) attached to both sides of the wristband to ensure negligible pressure drops across the single cell. The building's integrated compressed air supply was connected to a manual pressure regulator (PR364, Parker Hannifin) set to 1.5 bar, directly preceding an electropneumatic proportional regulator (8083T1, McMaster-Carr) which pressurized a 2-L accumulator (NY-16, NYAIR) to dampen fluctuations in pressure. For static analysis (steady-state forces and transient responses), the pressurized air leading to the wristband was gated by a 2-position, 3-way solenoid valve (VT307-5DZ1-02N-F, SMC Pneumatics). For dynamic analysis (frequency bandwidth), high-frequency (rated for 1,200 Hz) solenoids (SX12-AG, SMC Pneumatics) were placed on either side of the wristband, one for allowing pressurized air into the cell and the other for exhausting the pressurized air downstream of the cell. All wristbands were characterized with at least three trials, except for the 25-mm cell during dynamic testing, which has data for two trials. The electronics were controlled by a data acquisition unit (DAQ) (Q8-USB, Quanser) and were programmed through scripts written in C++. The wrist rig and electropneumatic circuits are detailed in the Supplemental Text and viewable in Figures S3 and S19–S22.

Characterization of Multi-Cell Sleeves

The multi-cell sleeves (Figure 3A) were fed building-supplied compressed air through a manual pressure regulator (PR364, Parker Hannifin) set to 1.5 bar, which preceded an electropneumatic proportional regulator (8083T2, McMaster-Carr). Three solenoid valves (VT307-5DZ1-02N-F, SMC Pneumatics) gated the pressurized air to the cells. The solenoids and regulator were controlled by a National Instruments (NI) DAQ (USB-6002). At a port in each cell, a pressure sensor (ADP5151, Panasonic) provided analog voltages to the DAQ, which was programmed by MATLAB scripts (version R2022a, MathWorks).

Characterization of Modules with Material-Based Fluidic Programming

The modules with textile-embedded control were similarly fed building-suppled compressed air and regulated by a manual pressure regulator (PR364, Parker Hannifin) set to 1 bar and verified by an electronic pressure gauge (MG1-30-A-9V-R, SSI Technologies). The pressurized air was gated by a solenoid valve (VT307-5DZ1-02N-F, SMC Pneumatics) and was measured at each cell by a pressure sensor (ADP5151, Panasonic) which provided analog voltages to an NI DAQ (USB-6002), programmed by MATLAB scripts (version R2022a, MathWorks).

The resistive open-cell polyurethane foam integrated into the module was first characterized separately for its fluidic sheet resistance as described in prior work.[68] Based on the measured sheet resistance of 5.7×10^9 kg m^{-4} s^{-1}, the numerical model was used to estimate the required annular geometry (see Supplemental Text on fluidic resistors) to provide the desired temporal delay in the point-force cues. To verify that the specified geometry of the resistor would provide the required resistance in practice, separate single-resistor components were fabricated and characterized with a pulse-width-modulated flow valve (2555N12, McMaster-Carr) for delivering a regulated flow rate, a flow meter (FLR1002-D, Omega) measuring the flow rate, and a pressure sensor (ADP5151, Panasonic). The electronic signals were provided by or delivered to an NI DAQ (USB-

6210) programmed to output a value for the fluidic resistance of the component as prescribed by scripts in MATLAB (version R2022a, MathWorks).

Experimental Procedure and Data Analysis for Participants in Efficacy Study
Participants (n = 14, 6 female, 12 right-handed, aged 20–27 years, averaging 23 years old) were recruited through publicly advertised flyers posted on the campus of Rice University (Houston, TX). Following the protocol approved by the Rice University's Institutional Review Board (IRB-FY2019-49), the participants were informed of the experimental procedure and signed a consent form for their haptic data to be used in this study and future studies. The experiment (including training and recorded data) lasted 1 hour per participant, beginning with informing the participant about the way that the cues progressed along the forearm. 20 cues (5 of each directional cue) were then delivered for training in a randomized order, during which the experimenter would provide the cue and the participant would respond with the perceived cue (forward, backward, left, or right), after which the experimenter provided the correct response to the participant. The participant would then don headphones playing pink noise (Dalesnale – Noise Ambient, YouTube) to prevent auditory feedback from the solenoid valves, and their arms were covered with an opaque sheet to occlude any visual feedback from watching the cells progressively inflate. After setup and training, the participant received 80 cues (20 for each direction) in a randomized order. The participant orally relayed the perceived cue to the experimenter who recorded their response without confirmation of accuracy.

The two sleeves had two pneumatic inputs each. The four pneumatic lines were gated by an array of solenoid valves in a manifold (SYJ314M-6LU-M5, SMC Pneumatics) controlled by a DAQ (Q8-USB, Quanser). The pressurized air originated from the building's supply of compressed air, regulated first by a manual pressure regulator (PR364, Parker Hannifin) set to 1.5 bar and then regulated downstream by an electropneumatic regulator (8083T1, McMaster-Carr) that fed into a 2-L accumulator (NY-16, NYAIR) upstream of the solenoid valves.

Experimental Procedure for Real-World Demonstrations
The haptic sleeves used for the untethered demonstrations were integrated into a long-sleeved compression shirt (NT8073, Neleus) sized for the user. Pneumatic tubing was routed under the shirt sleeves and connected to four miniature solenoids (LHDA0531115H, Lee Company) actuated by four n-channel MOSFET transistors (IRLZ14PBF-BE3, Vishay) and controlled by an Arduino Nano microcontroller (programmed through Arduino IDE), all of which were soldered to a "protoboard" (ECPB_H_BK'_5P, ElectroCookie). A 4-channel 433-MHz wireless receiver delivered electronic inputs to the microcontroller when a button was pressed on a paired 4-channel wireless transmitter (RX480E-4/TX118S-4, KOSEL Electronic Technology). The protoboard, a 1200-mAh 9-V battery (90693, Tenergy), and a pressure regulator (B07NRD1BPJ, Luckeg) for threaded canisters (with either a 16-g [CO2-T16, Pro Bike Tool] or 25-g [GF-CO2-25G-5PK, Gorilla Force] canister of compressed CO_2 gas) were all secured by adhesive-backed hooked fasteners to an elastic belt with loop fasteners along the entire length (90441WN, VELCRO). GPS data was recorded on an iPhone 13 Pro (Apple) with the OpenGPX application. The resulting GPS data was exported to MATLAB and processed with the geoscatter functions in version R2022a (MathWorks).

The user was instructed to walk in accordance with the haptic direction that they perceived through the textile sleeve. As the 4-button wireless remote could deliver signals up to 100 m, the experimenter pressing the buttons (each button corresponding to a directional haptic cue) was physically distanced from the user, and in the case of "drawing" the tetrominoes was often out of audible speaking range. For the waypoint-based navigation, the participant was unaware of the destination and the predetermined route prior to the experiment. The user walked to the first waypoint and operated a scooter to reach the second waypoint, in both cases with the videographer and experimenter primarily following behind. The user was instructed that the cues would be given approximately 5 m before each junction in the sidewalk and that a backward cue indicated the end of the route. For drawing the tetrominoes in an open field, the participant was told to start at an initial coordinate point (defined by a grid of cones spread 7 m apart) and directed via haptic cues to walk the predetermined shape (of which the user was unaware prior to the experiment). The wireless signal was delivered to the user at the beginning of each shape and approximately halfway between each successive cone that the user approached. A backward cue was sent to indicate that the participant was approaching the last cone, and two backward cues in rapid succession indicated a 180° turn, as shown in Figure S18.

Testing the Robustness of Modules with Material-Based Fluidic Programming
Prior to washing, the module first had the pressure response of each cell recorded as described in the characterization procedure of the device detailed above. The module had its ports sealed with Luer lock connectors and was secured in a laundry bag (MS87-350-004-17, Mainstays) and placed in a washing machine (WA51A5505AC/US, Samsung Electronics) with approximately 10 other garments. The washing machine was loaded with laundry detergent (Tide Free and Gentle, Procter & Gamble) and set to a delicate cycle with the coldest temperature, lowest soil level, and one rinse cycle. The module was washed 5 times and then had its pressure response recorded for each cell after drying for approximately 5–24 hours. This process was repeated for 25 washes (Figure 6M).

On the same device that was washed, we cut open cell C2 (Movie S4) and recorded the pressure response of each cell. A 20-mm diameter patch of the same HST material used to make the device was cut by a concentric hollow punch (66004, Mayhew Steel Products) and ironed on to the device with a household iron (D2030, Black + Decker), set to the "linen" setting and pressed by hand for approximately 30 seconds. The pressure response of each cell was then recorded again (Figure 6N).

Supplemental Information

    Supplemental Text
    Table S1
    Figures S1 to S29
    Movies S1 to S4
    Supplemental References

Author contributions

Conceptualization, B.J., Z.A.Z., M.K.O., and D.J.P.; Methodology, B.J., Z.A.Z., A.Y., A.R., M.K.O., and D.J.P.; Investigation, B.J., Z.A.Z., A.Y., A.R., D.X., T.F.Y., N.F., and Z.L.; Visualization, B.J., Z.A.Z., A.R., T.F.Y., and Z.L.; Funding Acquisition, B.J., Z.A.Z., A.R., M.K.O., and D.J.P.; Project Administration, B.J., Z.A.Z., M.K.O., and D.J.P.; Supervision, M.K.O., and D.J.P.; Writing – Original Draft, B.J. and D.J.P.; Writing – Review & Editing, B.J., Z.A.Z., A.Y., A.R., D.X., T.F.Y., N.F., Z.L., M.K.O., and D.J.P.

Declaration of interests: The authors declare that they have no competing interests.

Data and materials availability: All data are available in the main text or the supplemental information.

References

1. Bourne, R., and GBD 2019 Blindness and Vision Impairment Collaborators (2021). Trends in Prevalence of Blindness and Distance and Near Vision Impairment over 30 Years: An Analysis for the Global Burden of Disease Study. The Lancet Global Health *9*, e130–e143. 10.1016/S2214-109X(20)30425-3.

2. World Health Organization (2021). World Report on Hearing: Executive Summary (World Health Organization).

3. Chinello, F., Pacchierotti, C., Bimbo, J., Tsagarakis, N.G., and Prattichizzo, D. (2018). Design and Evaluation of a Wearable Skin Stretch Device for Haptic Guidance. IEEE Robotics and Automation Letters *3*, 524–531. 10.1109/LRA.2017.2766244.

4. Barontini, F., Catalano, M.G., Pallottino, L., Leporini, B., and Bianchi, M. (2021). Integrating Wearable Haptics and Obstacle Avoidance for the Visually Impaired in Indoor Navigation: A User-Centered Approach. IEEE Transactions on Haptics *14*, 109–122. 10.1109/TOH.2020.2996748.

5. Jiang, T., Qiu, W., Li, Z., Ye, X., Liu, Y., Li, Y., Wang, X., Zhong, J., Qian, X., and Lin, L. (2022). Programmable Tactile Feedback Patterns for Cognitive Assistance by Flexible Electret Actuators. Advanced Functional Materials *32*, 2107985. 10.1002/adfm.202107985.

6. Rhienmora, P., Gajananan, K., Haddawy, P., Dailey, M.N., and Suebnukarn, S. (2010). Augmented Reality Haptics System for Dental Surgical Skills Training. In Proceedings of the 17th ACM Symposium on Virtual Reality Software and Technology VRST '10. (Association for Computing Machinery), pp. 97–98. 10.1145/1889863.1889883.

7. Lipomi, D.J., Dhong, C., Carpenter, C.W., Root, N.B., and Ramachandran, V.S. (2020). Organic Haptics: Intersection of Materials Chemistry and Tactile Perception. Advanced Functional Materials *30*, 1906850. 10.1002/adfm.201906850.

8. Keef, C.V., Kayser, L.V., Tronboll, S., Carpenter, C.W., Root, N.B., Finn III, M., O'Connor, T.F., Abuhamdieh, S.N., Davies, D.M., Runser, R., et al. (2020). Virtual Texture Generated Using Elastomeric Conductive Block Copolymer in a Wireless Multimodal Haptic Glove. Advanced Intelligent Systems *2*, 2000018. 10.1002/aisy.202000018.

9. Rognon, C., Koehler, M., Duriez, C., Floreano, D., and Okamura, A.M. (2019). Soft Haptic Device to Render the Sensation of Flying Like a Drone. IEEE Robotics and Automation Letters *4*, 2524–2531. 10.1109/LRA.2019.2907432.

10. Yu, X., Xie, Z., Yu, Y., Lee, J., Vazquez-Guardado, A., Luan, H., Ruban, J., Ning, X., Akhtar, A., Li, D., et al. (2019). Skin-Integrated Wireless Haptic Interfaces for Virtual and Augmented Reality. Nature *575*, 473–479. 10.1038/s41586-019-1687-0.

11. Jadhav, S., Majit, M.R.A., Shih, B., Schulze, J.P., and Tolley, M.T. (2022). Variable Stiffness Devices Using Fiber Jamming for Application in Soft Robotics and Wearable Haptics. Soft Robotics *9*, 173–186. 10.1089/soro.2019.0203.

12. Yohanan, S., and MacLean, K.E. (2012). The Role of Affective Touch in Human-Robot Interaction: Human Intent and Expectations in Touching the Haptic Creature. Int J of Soc Robotics *4*, 163–180. 10.1007/s12369-011-0126-7.

13. Scheggi, S., Chinello, F., and Prattichizzo, D. (2012). Vibrotactile Haptic Feedback for Human-Robot Interaction in Leader-Follower Tasks. In Proceedings of the 5th International Conference on PErvasive Technologies Related to Assistive Environments PETRA '12. (Association for Computing Machinery), pp. 1–4. 10.1145/2413097.2413161.

14. Goodrich, M.A., and Schultz, A.C. (2008). Human–Robot Interaction: A Survey. HCI *1*, 203–275. 10.1561/1100000005.

15. Carrozza, M.C., Persichetti, A., Laschi, C., Vecchi, F., Lazzarini, R., Tamburrelli, V., Vacalebri, P., and Dario, P. (2005). A Novel Wearable Interface for Robotic Hand Prostheses. In 9th International Conference on Rehabilitation Robotics, 2005. ICORR 2005., pp. 109–112. 10.1109/ICORR.2005.1501063.

16. Kapusta, A., Yu, W., Bhattacharjee, T., Liu, C.K., Turk, G., and Kemp, C.C. (2016). Data-Driven Haptic Perception for Robot-Assisted Dressing. In 2016 25th IEEE International Symposium on Robot and Human Interactive Communication (RO-MAN), pp. 451–458. 10.1109/ROMAN.2016.7745158.

17. Theriault, A., Nagurka, M., and Johnson, M.J. (2014). Design and Development of an Affordable Haptic Robot with Force-Feedback and Compliant Actuation to Improve Therapy for Patients with Severe Hemiparesis. IEEE Transactions on Haptics *7*, 161–174. 10.1109/TOH.2013.51.

18. Thomas, N., Fazlollahi, F., Brown, J.D., and Kuchenbecker, K.J. (2021). Sensorimotor-inspired Tactile Feedback and Control Improve Consistency of Prosthesis Manipulation in the Absence of Direct Vision. In 2021 IEEE/RSJ International Conference on Intelligent Robots and Systems (IROS), pp. 6174–6181. 10.1109/IROS51168.2021.9635885.

19. Cianchetti, M., Laschi, C., Menciassi, A., and Dario, P. (2018). Biomedical Applications of Soft Robotics. Nat Rev Mater *3*, 143–153. 10.1038/s41578-018-0022-y.

20. O'Malley, M.K., and Gupta, A. (2008). Haptic Interfaces. In HCI Beyond the GUI (Elsevier), pp. 25–73. 10.1016/B978-0-12-374017-5.00002-X.

21. Jones, L.A., and Tan, H.Z. (2013). Application of Psychophysical Techniques to Haptic Research. IEEE Transactions on Haptics *6*, 268–284. 10.1109/TOH.2012.74.

22. Hale, K.S., and Stanney, K.M. (2004). Deriving Haptic Design Guidelines from Human Physiological, Psychophysical, and Neurological Foundations. IEEE Computer Graphics and Applications *24*, 33–39. 10.1109/MCG.2004.1274059.

23. Demain, S., Metcalf, C.D., Merrett, G.V., Zheng, D., and Cunningham, S. (2013). A Narrative Review on Haptic Devices: Relating the Physiology and Psychophysical Properties of the Hand to Devices for Rehabilitation in Central Nervous System Disorders. Disability and Rehabilitation: Assistive Technology *8*, 181–189. 10.3109/17483107.2012.697532.

24. Pezent, E., O'Malley, M.K., Israr, A., Samad, M., Robinson, S., Agarwal, P., Benko, H., and Colonnese, N. (2020). Explorations of Wrist Haptic Feedback for AR/VR Interactions with Tasbi. In Extended Abstracts of the 2020 CHI Conference on Human Factors in Computing Systems CHI EA '20. (Association for Computing Machinery), pp. 1–4. 10.1145/3334480.3383151.

25. Delazio, A., Nakagaki, K., Klatzky, R.L., Hudson, S.E., Lehman, J.F., and Sample, A.P. (2018). Force Jacket: Pneumatically-Actuated Jacket for Embodied Haptic Experiences. In Proceedings of the 2018 CHI Conference on Human Factors in Computing Systems (Association for Computing Machinery), pp. 1–12.

26. Pezent, E., Israr, A., Samad, M., Robinson, S., Agarwal, P., Benko, H., and Colonnese, N. (2019). Tasbi: Multisensory Squeeze and Vibrotactile Wrist Haptics for Augmented and Virtual Reality. In 2019 IEEE World Haptics Conference (WHC), pp. 1–6. 10.1109/WHC.2019.8816098.

27. Pezent, E., Agarwal, P., Hartcher-O'Brien, J., Colonnese, N., and O'Malley, M.K. (2022). Design, Control, and Psychophysics of Tasbi: A Force-Controlled Multimodal Haptic Bracelet. IEEE Transactions on Robotics, 1–17. 10.1109/TRO.2022.3164840.

28. Sullivan, J.L., Dunkelberger, N., Bradley, J., Young, J., Israr, A., Lau, F., Klumb, K., Abnousi, F., and O'Malley, M.K. (2020). Multi-Sensory Stimuli Improve Distinguishability of Cutaneous Haptic Cues. IEEE Transactions on Haptics *13*, 286–297. 10.1109/TOH.2019.2922901.

29. Shull, P.B., and Damian, D.D. (2015). Haptic Wearables as Sensory Replacement, Sensory Augmentation and Trainer – A Review. J NeuroEngineering Rehabil *12*, 59. 10.1186/s12984-015-0055-z.

30. Song, S., Noh, G., Yoo, J., Oakley, I., Cho, J., and Bianchi, A. (2015). Hot & Tight: Exploring Thermo and Squeeze Cues Recognition on Wrist Wearables. In Proceedings of the 2015 ACM International Symposium on Wearable Computers ISWC '15. (Association for Computing Machinery), pp. 39–42. 10.1145/2802083.2802092.

31. Prattichizzo, D., Otaduy, M., Kajimoto, H., and Pacchierotti, C. (2019). Wearable and Hand-Held Haptics. IEEE Transactions on Haptics *12*, 227–231. 10.1109/TOH.2019.2936736.

32. Dong, M., Fang, B., Li, J., Sun, F., and Liu, H. (2021). Wearable Sensing Devices for Upper Limbs: A Systematic Review. Proc Inst Mech Eng H *235*, 117–130. 10.1177/0954411920953031.

33. Dunkelberger, N., Sullivan, J.L., Bradley, J., Manickam, I., Dasarathy, G., Baraniuk, R., and O'Malley, M.K. (2021). A Multisensory Approach to Present Phonemes as Language Through a Wearable Haptic Device. IEEE Trans. Haptics *14*, 188–199. 10.1109/TOH.2020.3009581.

34. Yin, J., Hinchet, R., Shea, H., and Majidi, C. (2021). Wearable Soft Technologies for Haptic Sensing and Feedback. Adv. Funct. Mater. *31*, 2007428. 10.1002/adfm.202007428.

35. Maeda, T., Yoshida, S., Murakami, T., Matsuda, K., Tanikawa, T., and Sakai, H. (2022). Fingeret: A Wearable Fingerpad-Free Haptic Device for Mixed Reality. In Proceedings of the 2022 ACM Symposium on Spatial User Interaction SUI '22. (Association for Computing Machinery), pp. 1–10. 10.1145/3565970.3567703.

36. Zhang, B., and Sra, M. (2021). PneuMod: A Modular Haptic Device with Localized Pressure and Thermal Feedback. In Proceedings of the 27th ACM Symposium on Virtual Reality Software and Technology (ACM), pp. 1–7. 10.1145/3489849.3489857.

37. Hamdan, N.A., Wagner, A., Voelker, S., Steimle, J., and Borchers, J. (2019). Springlets: Expressive, Flexible and Silent On-Skin Tactile Interfaces. In Proceedings of the 2019 CHI Conference on Human Factors in Computing Systems (ACM), pp. 1–14. 10.1145/3290605.3300718.

38. Jung, Y.H., Yoo, J.-Y., Vázquez-Guardado, A., Kim, J.-H., Kim, J.-T., Luan, H., Park, M., Lim, J., Shin, H.-S., Su, C.-J., et al. (2022). A Wireless Haptic Interface for Programmable Patterns of Touch Across Large Areas of the Skin. Nat Electron *5*, 374–385. 10.1038/s41928-022-00765-3.

39. Jumet, B., Bell, M.D., Sanchez, V., and Preston, D.J. (2022). A Data-Driven Review of Soft Robotics. Advanced Intelligent Systems *4*, 2100163. 10.1002/aisy.202100163.

40. Sanchez, V., Payne, C.J., Preston, D.J., Alvarez, J.T., Weaver, J.C., Atalay, A.T., Boyvat, M., Vogt, D.M., Wood, R.J., Whitesides, G.M., et al. (2020). Smart Thermally Actuating Textiles. Advanced Materials Technologies *5*, 2000383. 10.1002/admt.202000383.

41. Sanchez, V., Walsh, C.J., and Wood, R.J. (2021). Textile Technology for Soft Robotic and Autonomous Garments. Advanced Functional Materials *31*, 2008278. 10.1002/adfm.202008278.

42. Pacchierotti, C., Sinclair, S., Solazzi, M., Frisoli, A., Hayward, V., and Prattichizzo, D. (2017). Wearable Haptic Systems for the Fingertip and the Hand: Taxonomy, Review, and Perspectives. IEEE Transactions on Haptics *10*, 580–600. 10.1109/TOH.2017.2689006.

43. Lee, D.-Y., Jeong, S.H., Cohen, A.J., Vogt, D.M., Kollosche, M., Lansberry, G., Mengüç, Y., Israr, A., Clarke, D.R., and Wood, R.J. (2022). A Wearable Textile-Embedded Dielectric Elastomer Actuator Haptic Display. Soft Robotics. 10.1089/soro.2021.0098.

44. Jumet, B., Zook, Z.A., Xu, D., Fino, N., Rajappan, A., Schara, M.W., Berning, J., Escobar, N., O'Malley, M.K., and Preston, D.J. (2022). A Textile-Based Approach to Wearable Haptic Devices. In 2022 IEEE 5th International Conference on Soft Robotics (RoboSoft) (IEEE), pp. 741–746. 10.1109/RoboSoft54090.2022.9762149.

45. Aggravi, M., Pausé, F., Giordano, P.R., and Pacchierotti, C. (2018). Design and Evaluation of a Wearable Haptic Device for Skin Stretch, Pressure, and Vibrotactile Stimuli. IEEE Robotics and Automation Letters *3*, 2166–2173. 10.1109/LRA.2018.2810887.

46. Raitor, M., Walker, J.M., Okamura, A.M., and Culbertson, H. (2017). WRAP: Wearable, Restricted-Aperture Pneumatics for Haptic Guidance. In 2017 IEEE International Conference on Robotics and Automation (ICRA), pp. 427–432. 10.1109/ICRA.2017.7989055.

47. Gohlke, K., Sattler, W., and Hornecker, E. (2022). AirPinch – An Inflatable Touch Fader with Pneumatic Tactile Feedback. In Sixteenth International Conference on Tangible, Embedded, and Embodied Interaction (ACM), pp. 1–6. 10.1145/3490149.3505568.

48. Young, E.M., Memar, A.H., Agarwal, P., and Colonnese, N. (2019). Bellowband: A Pneumatic Wristband for Delivering Local Pressure and Vibration. In 2019 IEEE World Haptics Conference (WHC), pp. 55–60. 10.1109/WHC.2019.8816075.

49. Zhu, M., Memar, A.H., Gupta, A., Samad, M., Agarwal, P., Visell, Y., Keller, S.J., and Colonnese, N. (2020). PneuSleeve: In-fabric Multimodal Actuation and Sensing in a Soft,

Compact, and Expressive Haptic Sleeve. In Proceedings of the 2020 CHI Conference on Human Factors in Computing Systems (ACM), pp. 1–12. 10.1145/3313831.3376333.

50. Wu, W., and Culbertson, H. (2019). Wearable Haptic Pneumatic Device for Creating the Illusion of Lateral Motion on the Arm. In 2019 IEEE World Haptics Conference (WHC), pp. 193–198. 10.1109/WHC.2019.8816170.

51. Goetz, D.T., Owusu-Antwi, D.K., and Culbertson, H. (2020). PATCH: Pump-Actuated Thermal Compression Haptics. In 2020 IEEE Haptics Symposium (HAPTICS), pp. 643–649. 10.1109/HAPTICS45997.2020.ras.HAP20.32.c4048ec3.

52. Culbertson, H., Nunez, C.M., Israr, A., Lau, F., Abnousi, F., and Okamura, A.M. (2018). A social haptic device to create continuous lateral motion using sequential normal indentation. In 2018 IEEE Haptics Symposium (HAPTICS), pp. 32–39. 10.1109/HAPTICS.2018.8357149.

53. Liu, Y., Nishikawa, S., Seong, Y. ah, Niiyama, R., and Kuniyoshi, Y. (2021). ThermoCaress: A Wearable Haptic Device with Illusory Moving Thermal Stimulation. In Proceedings of the 2021 CHI Conference on Human Factors in Computing Systems (ACM), pp. 1–12. 10.1145/3411764.3445777.

54. Uramune, R., Ishizuka, H., Hiraki, T., Kawahara, Y., Ikeda, S., and Oshiro, O. (2022). HaPouch: A Miniaturized, Soft, and Wearable Haptic Display Device Using a Liquid-to-Gas Phase Change Actuator. IEEE Access *10*, 16830–16842. 10.1109/ACCESS.2022.3141385.

55. Endow, S., Moradi, H., Srivastava, A., Noya, E.G., and Torres, C. (2021). Compressables: A Haptic Prototyping Toolkit for Wearable Compression-based Interfaces. In Designing Interactive Systems Conference 2021 DIS '21. (Association for Computing Machinery), pp. 1101–1114. 10.1145/3461778.3462057.

56. Li, Z., Ma, Y., Zhang, K., Wan, J., Zhao, D., Pi, Y., Chen, G., Zhang, J., Tang, W., Lin, L., et al. (2023). Air Permeable Vibrotactile Actuators for Wearable Wireless Haptics. Advanced Functional Materials *33*, 2211146. 10.1002/adfm.202211146.

57. Ramachandran, V., Schilling, F., Wu, A.R., and Floreano, D. (2021). Smart Textiles that Teach: Fabric-Based Haptic Device Improves the Rate of Motor Learning. Advanced Intelligent Systems *3*, 2100043. 10.1002/aisy.202100043.

58. Dunkelberger, N., Bradley, J., Sullivan, J.L., Israr, A., Lau, F., Klumb, K., Abnousi, F., and O'Malley, M.K. (2018). Improving Perception Accuracy with Multi-sensory Haptic Cue Delivery. In Haptics: Science, Technology, and Applications Lecture Notes in Computer Science., D. Prattichizzo, H. Shinoda, H. Z. Tan, E. Ruffaldi, and A. Frisoli, eds. (Springer International Publishing), pp. 289–301. 10.1007/978-3-319-93399-3_26.

59. Hinchet, R., Vechev, V., Shea, H., and Hilliges, O. (2018). DextrES: Wearable Haptic Feedback for Grasping in VR via a Thin Form-Factor Electrostatic Brake. In Proceedings of the 31st Annual ACM Symposium on User Interface Software and Technology (ACM), pp. 901–912. 10.1145/3242587.3242657.

60. Gupta, A., Irudayaraj, A.A.R., and Balakrishnan, R. (2017). HapticClench: Investigating Squeeze Sensations using Memory Alloys. In Proceedings of the 30th Annual ACM

Symposium on User Interface Software and Technology (ACM), pp. 109–117. 10.1145/3126594.3126598.

61. Sonar, H.A., Huang, J.-L., and Paik, J. (2021). Soft Touch using Soft Pneumatic Actuator–Skin as a Wearable Haptic Feedback Device. Advanced Intelligent Systems *3*, 2000168. 10.1002/aisy.202000168.

62. Pohl, H., Brandes, P., Ngo Quang, H., and Rohs, M. (2017). Squeezeback: Pneumatic Compression for Notifications. In Proceedings of the 2017 CHI Conference on Human Factors in Computing Systems (ACM), pp. 5318–5330. 10.1145/3025453.3025526.

63. Fino, N., Jumet, B., Zook, Z.A., Preston, D.J., and O'Malley, M.K. (2023). Mechanofluidic Instability-Driven Wearable Textile Vibrotactor. IEEE Transactions on Haptics, 1–6. 10.1109/TOH.2023.3271128.

64. Wehner, M., Truby, R.L., Fitzgerald, D.J., Mosadegh, B., Whitesides, G.M., Lewis, J.A., and Wood, R.J. (2016). An integrated design and fabrication strategy for entirely soft, autonomous robots. Nature *536*, 451–455. 10.1038/nature19100.

65. Hubbard, J.D., Acevedo, R., Edwards, K.M., Alsharhan, A.T., Wen, Z., Landry, J., Wang, K., Schaffer, S., and Sochol, R.D. (2021). Fully 3D-printed soft robots with integrated fluidic circuitry. Science Advances *7*, eabe5257. 10.1126/sciadv.abe5257.

66. Preston, D.J., Jiang, H.J., Sanchez, V., Rothemund, P., Rawson, J., Nemitz, M.P., Lee, W.-K., Suo, Z., Walsh, C.J., and Whitesides, G.M. (2019). A Soft Ring Oscillator. Science Robotics *4*. 10.1126/scirobotics.aaw5496.

67. Rothemund, P., Ainla, A., Belding, L., Preston, D.J., Kurihara, S., Suo, Z., and Whitesides, G.M. (2018). A Soft, Bistable Valve for Autonomous Control of Soft Actuators. Science Robotics *3*, eaar7986. 10.1126/scirobotics.aar7986.

68. Rajappan, A., Jumet, B., Shveda, R.A., Decker, C.J., Liu, Z., Yap, T.F., Sanchez, V., and Preston, D.J. (2022). Logic-Enabled Textiles. Proceedings of the National Academy of Sciences *119*, e2202118119. 10.1073/pnas.2202118119.

69. Preston, D.J., Rothemund, P., Jiang, H.J., Nemitz, M.P., Rawson, J., Suo, Z., and Whitesides, G.M. (2019). Digital Logic for Soft Devices. Proceedings of the National Academy of Sciences *116*, 7750–7759. 10.1073/pnas.1820672116.

70. McDonald, K., and Ranzani, T. (2021). Hardware Methods for Onboard Control of Fluidically Actuated Soft Robots. Frontiers in Robotics and AI *8*.

71. Hoang, S., Karydis, K., Brisk, P., and Grover, W.H. (2021). A Pneumatic Random-Access Memory for Controlling Soft Robots. PLOS ONE *16*, e0254524. 10.1371/journal.pone.0254524.

72. Decker, C.J., Jiang, H.J., Nemitz, M.P., Root, S.E., Rajappan, A., Alvarez, J.T., Tracz, J., Wille, L., Preston, D.J., and Whitesides, G.M. (2022). Programmable Soft Valves for Digital and Analog Control. Proceedings of the National Academy of Sciences *119*, e2205922119. 10.1073/pnas.2205922119.

73. Vasios, N., Gross, A.J., Soifer, S., Overvelde, J.T.B., and Bertoldi, K. (2020). Harnessing Viscous Flow to Simplify the Actuation of Fluidic Soft Robots. Soft Robotics *7*, 1–9. 10.1089/soro.2018.0149.

74. Futran, C.C., Ceron, S., Murray, B.C.M., Shepherd, R.F., and Petersen, K.H. (2018). Leveraging fluid resistance in soft robots. In 2018 IEEE International Conference on Soft Robotics (RoboSoft), pp. 473–478. 10.1109/ROBOSOFT.2018.8405371.

75. Napp, N., Araki, B., Tolley, M.T., Nagpal, R., and Wood, R.J. (2014). Simple passive valves for addressable pneumatic actuation. In 2014 IEEE International Conference on Robotics and Automation (ICRA), pp. 1440–1445. 10.1109/ICRA.2014.6907041.

76. Koivikko, A., Lampinen, V., Pihlajamäki, M., Yiannacou, K., Sharma, V., and Sariola, V. (2022). Integrated Stretchable Pneumatic Strain Gauges for Electronics-Free Soft Robots. Commun Eng *1*, 1–10. 10.1038/s44172-022-00015-6.

77. Yasuda, H., Buskohl, P.R., Gillman, A., Murphey, T.D., Stepney, S., Vaia, R.A., and Raney, J.R. (2021). Mechanical computing. Nature *598*, 39–48. 10.1038/s41586-021-03623-y.

78. Drotman, D., Jadhav, S., Sharp, D., Chan, C., and Tolley, M.T. (2021). Electronics-free pneumatic circuits for controlling soft-legged robots. Science Robotics *6*, eaay2627. 10.1126/scirobotics.aay2627.

79. Laschi, C., and Wood, R.J. (2021). Smarter Materials for Smarter Robots. Science Robotics *6*, eabh4443. 10.1126/scirobotics.abh4443.

80. McDonald, K., Rendos, A., Woodman, S., Brown, K.A., and Ranzani, T. (2020). Magnetorheological Fluid-Based Flow Control for Soft Robots. Advanced Intelligent Systems *2*, 2000139. 10.1002/aisy.202000139.

81. Cacucciolo, V., Shintake, J., Kuwajima, Y., Maeda, S., Floreano, D., and Shea, H. (2019). Stretchable pumps for soft machines. Nature *572*, 516–519. 10.1038/s41586-019-1479-6.

82. El Helou, C., Grossmann, B., Tabor, C.E., Buskohl, P.R., and Harne, R.L. (2022). Mechanical Integrated Circuit Materials. Nature *608*, 699–703. 10.1038/s41586-022-05004-5.

83. Wehner, M., Tolley, M.T., Mengüç, Y., Park, Y.-L., Mozeika, A., Ding, Y., Onal, C., Shepherd, R.F., Whitesides, G.M., and Wood, R.J. (2014). Pneumatic Energy Sources for Autonomous and Wearable Soft Robotics. Soft Robotics *1*, 263–274. 10.1089/soro.2014.0018.

84. Shveda, R.A., Rajappan, A., Yap, T.F., Liu, Z., Bell, M.D., Jumet, B., Sanchez, V., and Preston, D.J. (2022). A Wearable Textile-Based Pneumatic Energy Harvesting System for Assistive Robotics. Science Advances *8*, eabo2418. 10.1126/sciadv.abo2418.

85. Mountcastle, V.B., Talbot, W.H., Darian-Smith, I., and Kornhuber, H.H. (1967). Neural Basis of the Sense of Flutter-Vibration. Science *155*, 597–600. 10.1126/science.155.3762.597.

86. Nakamura, A., Yamada, T., Goto, A., Kato, T., Ito, K., Abe, Y., Kachi, T., and Kakigi, R. (1998). Somatosensory Homunculus as Drawn by MEG. NeuroImage *7*, 377–386. 10.1006/nimg.1998.0332.

87. Nolan, M.F. (1982). Two-Point Discrimination Assessment in the Upper Limb in Young Adult Men and Women. Physical Therapy *62*, 965–969. 10.1093/ptj/62.7.965.

88. Nunez, C.M., Huerta, B.N., Okamura, A.M., and Culbertson, H. (2020). Investigating Social Haptic Illusions for Tactile Stroking (SHIFTS). In 2020 IEEE Haptics Symposium (HAPTICS), pp. 629–636. 10.1109/HAPTICS45997.2020.ras.HAP20.35.f631355d.

89. Helson, H. (1930). The Tau Effect—an Example of Psychological Relativity. Science *71*, 536–537. 10.1126/science.71.1847.536.

90. Geldard, F.A., and Sherrick, C.E. (1972). The Cutaneous "Rabbit": A Perceptual Illusion. Science *178*, 178–179. 10.1126/science.178.4057.178.

91. Goldreich, D. (2007). A Bayesian Perceptual Model Replicates the Cutaneous Rabbit and Other Tactile Spatiotemporal Illusions. PLOS ONE *2*, e333. 10.1371/journal.pone.0000333.

92. Brown, J.D., Paek, A., Syed, M., O'Malley, M.K., Shewokis, P.A., Contreras-Vidal, J.L., Davis, A.J., and Gillespie, R.B. (2013). Understanding the Role of Haptic Feedback in a Teleoperated/Prosthetic Grasp and Lift Task. In 2013 World Haptics Conference (WHC), pp. 271–276. 10.1109/WHC.2013.6548420.

93. Brown, J.D., Fernandez, J.N., Cohen, S.P., and Kuchenbecker, K.J. (2017). A Wrist-Squeezing Force-Feedback System for Robotic Surgery Training. In 2017 IEEE World Haptics Conference (WHC), pp. 107–112. 10.1109/WHC.2017.7989885.

94. Machaca, S., Ung, G., and Brown, J.D. (2020). Towards an Understanding of the Utility of Dual-Modality Haptic Feedback in Teleoperated Medical Devices. IEEE Transactions on Medical Robotics and Bionics *2*, 574–577. 10.1109/TMRB.2020.3034254.

95. Ramachandran, V., Macchini, M., and Floreano, D. (2022). Arm-Wrist Haptic Sleeve for Drone Teleoperation. IEEE Robotics and Automation Letters *7*, 12054–12061. 10.1109/LRA.2021.3122107.

96. Rognon, C., Ramachandran, V., Wu, A.R., Ijspeert, A.J., and Floreano, D. (2019). Haptic Feedback Perception and Learning with Cable-Driven Guidance in Exosuit Teleoperation of a Simulated Drone. IEEE Transactions on Haptics *12*, 375–385. 10.1109/TOH.2019.2925612.

97. Rognon, C., Koehler, M., Floreano, D., and Okamura, A.M. (2019). Perception of a Wearable Haptic Feedback Device to Render the Sensation of Flight. In 2019 IEEE World Haptics Conference (WHC), pp. 61–66. 10.1109/WHC.2019.8816126.

98. Bark, K., Wheeler, J.W., Premakumar, S., and Cutkosky, M.R. (2008). Comparison of Skin Stretch and Vibrotactile Stimulation for Feedback of Proprioceptive Information. In 2008 Symposium on Haptic Interfaces for Virtual Environment and Teleoperator Systems, pp. 71–78. 10.1109/HAPTICS.2008.4479916.

99. Hawkes, E.W., Majidi, C., and Tolley, M.T. (2021). Hard questions for soft robotics. Science Robotics *6*. 10.1126/scirobotics.abg6049.

100. Bettenhausen, C., Halford, B., Patel, P., Scott, A., and Vitale, G. (2022). The Future of Sustainable Textiles (American Chemical Society).

101. Mu, B., and Yang, Y. (2022). Complete Separation of Colorants from Polymeric Materials for Cost-Effective Recycling of Waste Textiles. Chemical Engineering Journal *427*, 131570. 10.1016/j.cej.2021.131570.

102. van Laake, L.C., de Vries, J., Malek Kani, S., and Overvelde, J.T.B. (2022). A Fluidic Relaxation Oscillator for Reprogrammable Sequential Actuation in Soft Robots. Matter *5*, 2898–2917. 10.1016/j.matt.2022.06.002.

Supplemental Text

Preload

Prior to collecting extensive force-pressure data, we analyzed the effect on steady-state forces of preloading magnitudes. A preloaded tightness of the wristband is necessary to ensure a consistent experimental procedure. We examined three different preloaded values (measured in the vertical axis) for each of the four geometries of the cell: 0.5, 1.0, and 1.5 N (**Figure S4**).

At 0.5-N preloads, the 30-mm cell far exceeded the force of the other three cells, disallowing for evenly spaced ranges of forces across the bands (**Figure S4A**). The wristbands preloaded to 1.5 N have the most even spacing of the ranges of forces (**Figure S4C**), but across 0–1 bar of pressure, no wristbands exerted a distribution of forces across 0–10 N, which was the desired range for comfortable force cues. For the 1.0-N preload (**Figure S4B**), we observed a 0–10-N range of forces for the 25-mm cell, and the other cells exhibited similar ranges of forces relative to each other.

Transient Response

We examined the transient responses of force for each size of cell to observe how closely each cell followed a step input of pressure, i.e., the response time (**Figure S5**). Generally, the wristbands followed closely and achieved a rise time of approximately 0.1 s. More specifically, a 3-dB attenuation is approximately a 50% reduction in force, and the time at which this cutoff frequency occurs for all four cells would be around 0.04–0.05 s, indicating that our cells could reach up to 20 Hz before non-negligible attenuation occurs, if the upstream solenoid valves were capable of such frequencies without fluidic losses. This transient response corroborates our findings that cycling at frequencies higher than 10–20 Hz attenuates the corresponding force. Overshoot likely occurs due to the compliant materials (e.g., the elastomeric "skin" and the strap of the wristband) dynamically distributing the force over the entirety of the wrist, but the response promptly settles in a time that is an order of magnitude less than the rise time.

Volume of an Inflated Rectangle

The maximum volume of a rectangular region enveloped by an inextensible membrane is also known as the "paper bag problem" or "teabag problem."[1-7] An exact analytical solution has not yet been determined. However, a generally agreed upon approximation is described in Equation S1,[7] where the maximum volume (V_{max}) is a cubic function of the shorter side (w) and the aspect ratio (l/w). Here, we use a rectangle of equal sides, where $w = l$, as the dimension for our cells; as such, V_{max} can be simplified to Equation S2.

$$V_{max} = w^3 \left(\frac{l}{\pi w} - 0.142 \left(1 - 10^{\frac{-l}{w}} \right) \right) \qquad (S1)$$

$$V_{max} = 0.190 w^3 \qquad (S2)$$

We measured the maximum volumes of the cells in our wristbands by using an electronic syringe pump (PHD 22/2000, Harvard Apparatus) to fill each device with Ecoflex 00-30 (Smooth-On) at a pressure of 1 bar, verified by a digital pressure gauge (MGA-30-A-9V-R, SSI

Technologies), and allowed to cure for 24 hours. We weighed the devices (seen in **Figure S6A**) before and after with an electronic scale (AX324, Ohaus). The volume of each device was then calculated by using the reported specific gravity of the elastomer and the corresponding differential weights of each device. The volumes of our cells are plotted against the model from Equation S2 in **Figure S7**.

We performed the same procedure for our programmed fluidic haptic module, but we modified the design (**Figure S8**) such that the cells and channels had approximately the same areal geometry but between only two layers (rather than three as in the original device). We made this change because the viscosity of the elastomer prevents the device from filling entirely due to the microporous structure of the open-cell foam and the flow between layers by way of vias. The resulting volume of the programmed module (including both cells and channels) is averaged over the three cells contained within the device (**Figure S7**). We used this average volume of 5.86 mL per cell, accounting for the added channel volume between cells in the system, as a physical reference for the fluidic capacitance in our models. In **Figure S9** we compare the predicted volume of a 25-mm cell (2.97 mL) without accounting for flow channels to the empirical volume of   5.86 mL in our numerical model. The results are functionally similar, but the 2.97-mL volume has a faster theoretical response than the empirical data collected for the fluidically programmed module. Alternatively, the 5.86-mL volume accurately follows the recorded pressure response.

Modeling of Resistors (Flow through Porous Media)

The fluidic resistors (**Figure 4C**) are fabricated from a 1.6-mm-thick open-cell polyurethane foam that is cut into concentric circles (i.e., an annulus). Long, thin serpentine channels between textile sheets serve as an alternative method to create pressure drops, but the foam is easier to integrate into our fabrication process because of its simplicity as a commercially available product, compactness relative to the area required for long serpentine paths, and analytically tractable resistance. The sheet resistance ($R_s = 5.7 \times 10^9$ kg m^{-4} s^{-1}) was measured as described in Experimental Procedures and is used to find the fluidic resistance (R, equal to pressure drop per unit flow rate) of the annulus as defined by Equation S3, where r_1 is the inner radius and r_2 is the outer radius. Analytically, R is calculated as 1.81×10^9 kg m^{-4} s^{-1}; we empirically determined R as 1.88×10^9 kg m^{-4} s^{-1} (**Figure 4D**), differing less than 4% from the expected value. We used the empirical value in our model.

$$R = \frac{R_s}{2\pi} \ln\left(\frac{r_2}{r_1}\right) \tag{S3}$$

The fluidic resistance of pipe (i.e., tube or channel) can be evaluated with the Hagen-Poiseuille equation (Equation S4), where μ is the dynamic viscosity of the fluid, L is the length of the pipe, and r is the radius of the pipe. If a pipe has a length on the order of 100 mm with a diameter on the order of 1 mm (the approximate dimensions of a channel within a sleeve), then the resistance would be 7.4×10^7 kg m^{-4} s^{-1}, two orders of magnitude less than the resistance of a single foam resistor. Thus, the effect of inter-cell channels or external tubing is negligible relative to the imposed fluidic resistance of the foam.

$$R = \frac{\Delta P}{Q} = \frac{8\mu L}{\pi r^4} \tag{S4}$$

Resistor-Capacitor Circuit Analysis of a Time-Variant Input

We used Ohm's law to find the voltages (V_1, V_2, V_3)—analogous to pressures—in each capacitor (i.e., cell) in response to a sinusoidal (alternating current) input. Equations S5–S7 provide the real (a) and imaginary (b) parts of each voltage, where $n = R_3 / R_2$, ω is angular frequency, the capacitance of each cell is defined by the ideal gas law $C_i = V_i / R_g T_g$, and $K = \omega R_2 C_i$. Lastly, we determine the attenuation (G) and phase lag (ϕ) from Equations S8, S9.

$$V_1 = V_3 \left[1 - nK^2 + i(2+n)K \right] \tag{S5}$$

$$V_2 = V_3 \left[1 + inK \right] \tag{S6}$$

$$V_3 = V_1 \frac{1 - nK^2 - i(2+n)K}{1 + (n^2 + 4)K^2 + n^2 K^4} \tag{S7}$$

$$G = 10 \log_{10} \left(\sqrt{a^2 + b^2} \right) \tag{S8}$$

$$\phi = \arctan\left(\frac{b}{a} \right) \tag{S9}$$

Table S1. Comparison of state-of-the-art wearable haptic devices. Demonstrated programmability is defined as having documented experimentation with changes (excluding on-off operations) in the amplitude, location, or timing of actuation after the initial setup and powering of the actuator; A: amplitudinal; S: spatial; T: temporal; ~: calculated or estimated values based on data provided in manuscript; --: the data was unreported or not found; PCB: printed circuit board; IC: integrated circuit.

Ref.	Cue	Forces	Tactile Bandwidth (3-dB cutoff)	Demonstrated Programmability	Mechanism of Actuation	Materials in Wearable Device (Actuator; attachment; controller)	Weight of Device	Embedded, On-Board, or Wearable Control
This work	Point-force	0–20 N	0–15 Hz	A, S, T	Inflatable volume	Textile; textile; textile, foam	6 g (single-cell wristband), 40 g (sleeve)	Embedded
(55)	Point-force	--	--	A, T	Inflatable volume	Elastomer; textile; --	--	--
(56)	Vibrotactile	0–60 mN	~0–1000 Hz	A, S, T	Electrostatic	Textile; textile; flexible composite	Unreported (actuators: 0.47 g/cm³)	On-board flexible PCB
(57)	Kinesthetic	~0–95 N	--	A	Electrostatic	Metalized thermoplastic sheet; textile, elastomer, and rigid plastic; --	Unreported (25 g per clutch)	--
(48)	Point-force	0–10 N	0–7 Hz	A, S, T	Inflatable volume	Thermoplastic sheet; textile; --	11 g	--
(58)	Compressive	588 mNm	--	--	Electromechanical	Rigid plastic, metal; textile; --	--	--
	Skin-stretch	375 mNm	--	--				
	Vibrotactile	--	--	S, T				
(45)	Compressive	2.5–10 N	--	A, T	Electromechanical	Rigid plastic, metal; textile; --	220 g	--
	Skin-stretch	--	--	A, T				
	Vibrotactile	--	--	S, T				
(59)	Kinesthetic	0–20 N	--	A, S, T	Electrostatic	Metal, polyimide film; textile and rigid plastic; --	8 g	--

Ref.	Cue	Forces	Tactile Bandwidth (3-dB cutoff)	Demonstrated Programmability	Mechanism of Actuation	Materials in Wearable Device (Actuator; attachment; controller)	Weight of Device	Embedded, On-Board, or Wearable Control
(35)	Skin-stretch	--	~0–20 Hz	A, T	Electromechanical	Rigid plastic, elastomer; plastic; rigid composite	18 g	On-board PCB
	Vibrotactile	--	~170 Hz	--				
(25)	Point-force	0.3–9 N	--	A, S, T	Inflatable volume	Thermoplastic sheet; textile; --	2.27 kg	--
(60)	Compressive	~0–16 N	--	A, S	Shape memory	Shape-memory alloy; textile; rigid composite	--	On-board PCB
(30)	Compressive	0.24–1.27 N	--	A, T	Electromechanical	Rigid plastic, metal; textile; rigid composite	--	On-board PCB
	Vibrotactile	--	--	T	Electromechanical			
	Thermal	--	--	A	Peltier effect			
(52)	Vibrotactile	1–2 N	~75–100 Hz	A, S, T	Electromechanical	Rigid plastic, metal; textile; --	Unreported (29 g per vibrotactor)	--
(51)	Compressive	--	--	S, T	Inflatable volume	Textile; textile; --	77.1–118.2 g	--
	Thermal	--	--	A, S, T	Fluidic heat exchanger			
(36)	Point-force	0–10 N	--	A, S, T	Inflatable volume	Elastomer, rigid composite; textile; --	--	--
	Thermal	--	--	A, S	Peltier effect			
(49)	Compressive	~0–1.6 N	~0–5 Hz	A, S, T	Inflatable volume	Elastomer; textile; --	26 g	--
	Skin-stretch	0–4 N	~0–5 Hz	A, S, T				
(10)	Vibrotactile	~135 mN	~150–250 Hz	A, S, T	Electromechanical	Metal; elastomer; flexible composite	38–130 g	On-board flexible IC
(9)	Point-force	0–20 N	--	A, S, T	Inflatable volume, electromechanical	Thermoplastic sheet, metal, rigid plastic; textile; rigid composite	--	Wearable hardware

Ref.	Cue	Forces	Tactile Bandwidth (3-dB cutoff)	Demonstrated Programmability	Mechanism of Actuation	Materials in Wearable Device (Actuator; attachment; controller)	Weight of Device	Embedded, On-Board, or Wearable Control
(61)	Point-force	0–0.3 N	0–90 Hz	A, S, T	Inflatable volume	Elastomer, compliant metal; elastomer; --	--	--
(37)	Skin-stretch	--	--	A, T	Shape memory	Shape-memory alloy; textile; --	--	--
(37)	Point-force	--	--	A	Shape memory	Shape-memory alloy; textile; --	--	--
(62)	Compressive	--	--	A, T	Inflatable volume	--; --; --	60 g	Wearable hardware
(53)	Point-force	--	--	A, S, T	Inflatable volume; heat exchanger	Textile; textile; --	--	--
(53)	Thermal	--	--	A, S, T	Inflatable volume; heat exchanger	Textile; textile; --	--	--
(50)	Point-force	--	--	A, S, T	Inflatable volume	Thermoplastic sheet; textile; --	--	--
(46)	Point-force	--	--	S, T	Inflatable volume	Thermoplastic sheet; textile; --	--	--
(38)	Vibrotactile	--	--	A, S, T	Electromechanical	Metal; elastomer; flexible composite	28.63 g	On-board flexible IC
(43)	Vibrotactile	~0–200 mN	7.5–240 Hz	A, S, T	Dielectric elastomeric actuator	Elastomer; textile; --	60 g	--
(63)	Vibrotactile	23–114 g	~183–200 Hz	A, T	Inflatable volume	Textile; textile; textile	9 g	Embedded
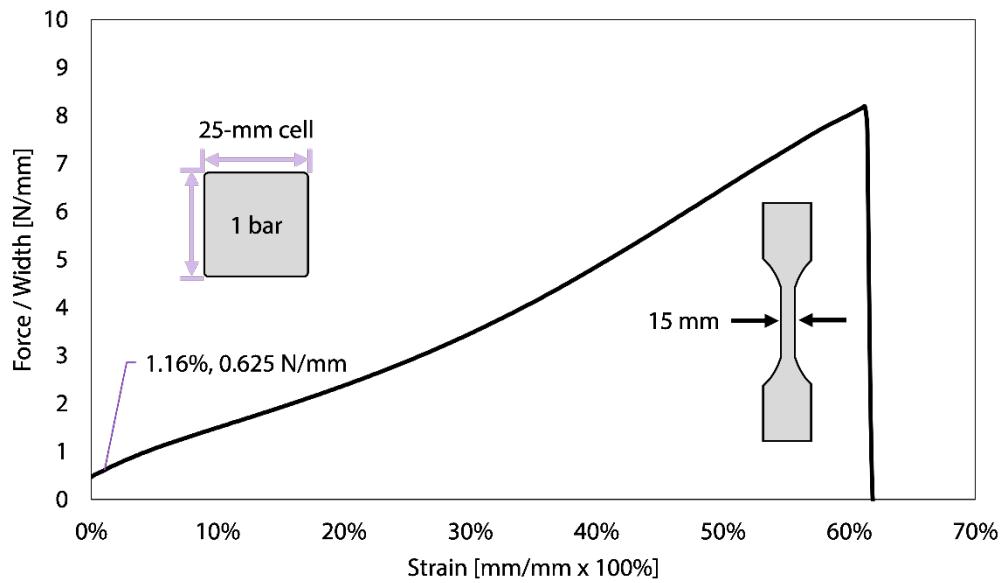
Figure S1. Inextensibility of the heat-sealable nylon taffeta. Using a universal test machine (68SC-2, Instron), we pulled a dog-bone sample of nylon taffeta and found the force per width as a function of strain. Pressurizing a 25-mm cell to 1 bar creates a force per width of 0.625 N/mm, which causes approximately a 1.16% strain on the material.
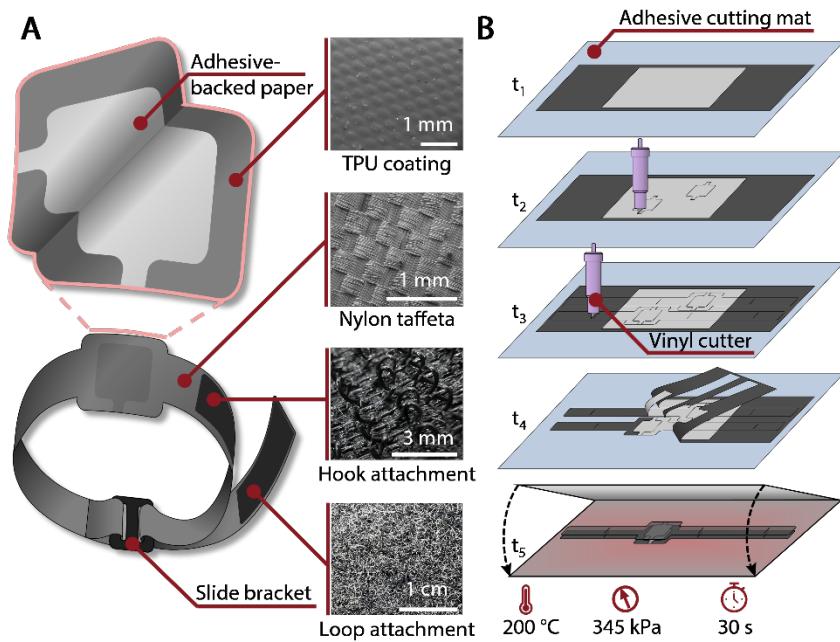
Figure S2. Design and fabrication of a single-cell wristband. (**A**) Wristband with an inflatable cell made from TPU-coated nylon taffeta, with adhesive-backed paper defining the internal geometry. The wristband is secured by hook-and-loop fasteners and made easily adjustable by adding a slide bracket. (**B**) Fabrication of a typical textile-based device from heat-sealable textiles shows the bondable and impermeable layers placed on a cutting mat (t_1), the vinyl cutter selectively cutting the top impermeable layer (t_2), a deeper cut outlining the textile layers (t_3), removal (i.e., weeding) of excess material (t_4), and heat pressing the layers together to form the thermal bond (t_5).
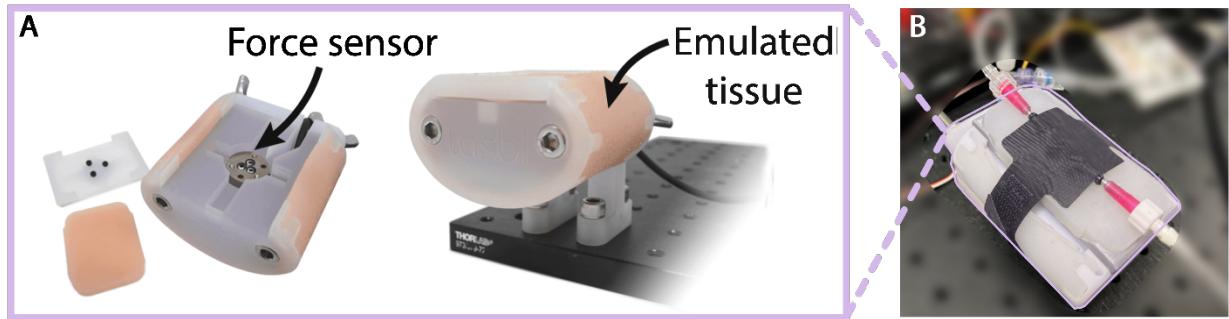
Figure S3. Instrumented test rig emulating a human wrist. (**A**) 3D-printed plastic inner portions emulate skeletal structures, and the elastomeric outer portions emulate human tissue. (**B**) A wristband is strapped around the instrumented test rig with pneumatic connections attached to either side. The endogenous Nano25 sensor recorded the force data as the cell inflated and reported to a data acquisition unit (Q8-USB, Quanser).
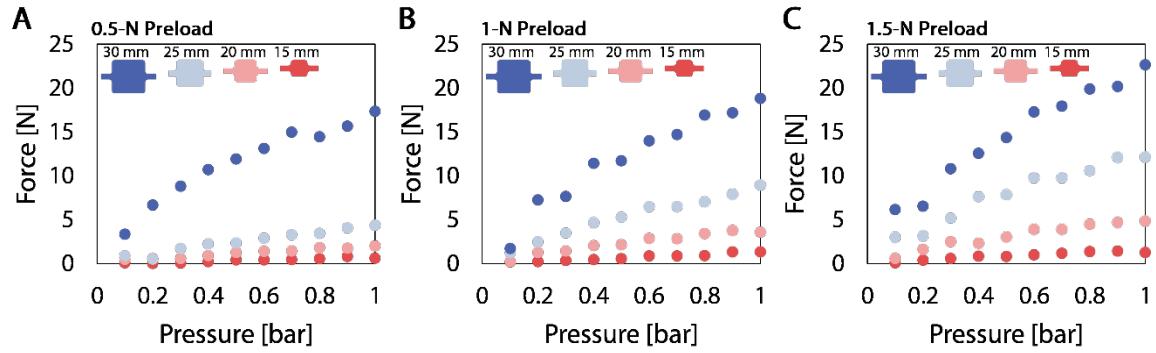
Figure S4. Different magnitudes of preload applied to each wristband to characterize the effect on steady-state forces across 0–1 bar of pressure. (**A**) With a 0.5-N preload, the 30-mm cell already exhibited more pressure than desired (i.e., 10 N), and the other sizes of cells were too low and similar in magnitude to each other. (**B**) The 1-N preload allowed for a reasonable distribution of forces across sizes of cells, and the 25-mm cell exhibited a 0–9.8-N range of forces, which is desired for tactile cues. (**C**) The 1.5-N preload created the most equally distributed range of forces across cells but did not have any of the cells within the desired range of 0–10 N across 0–1 bar.
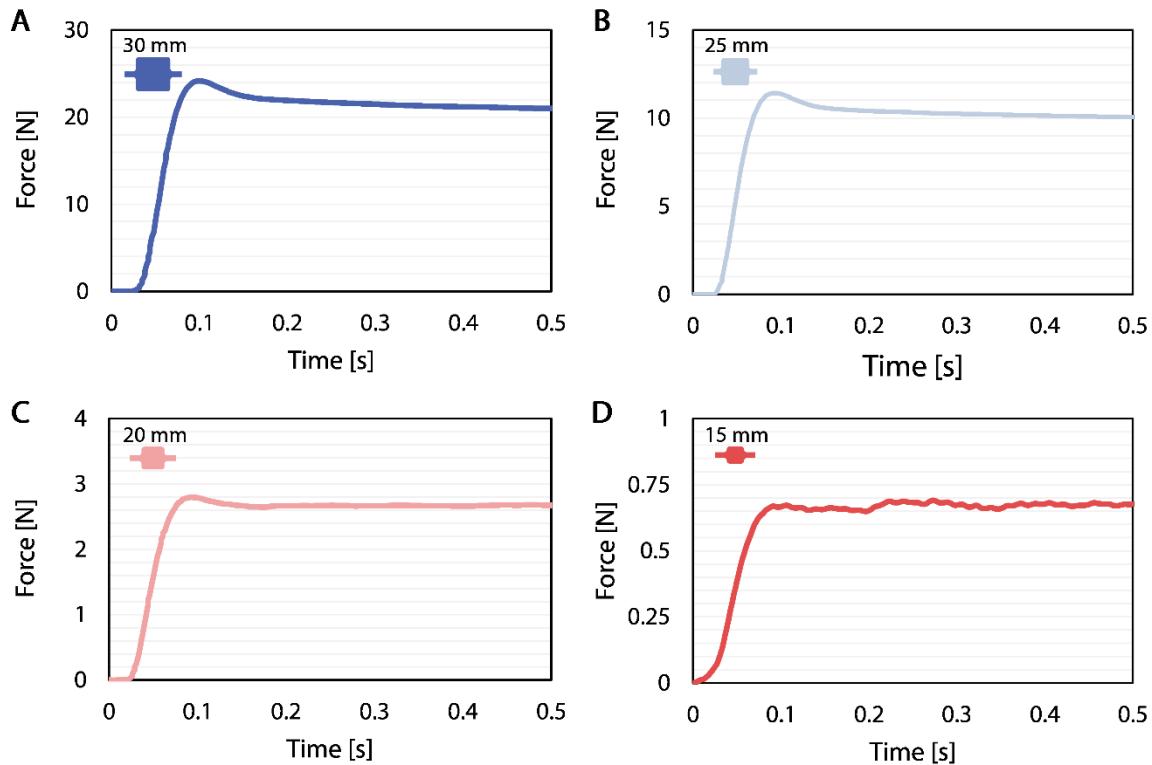
Figure S5. Transient response of each cell at step input of 1 bar of pressure. (**A**) 30-mm, (**B**) 25-mm, (**C**) 20-mm, and (**D**) 15-mm cells, with the corresponding forces recorded on the wrist rig (Figure S3) shown versus time after a step input of pressure. All sizes of cell reached a steady-state value within 0.1–0.2 s, but the larger cells tended to have more overshoot before settling. The dynamics of the system are more prevalent in the larger cells due to the larger accumulation of fluidic volume.
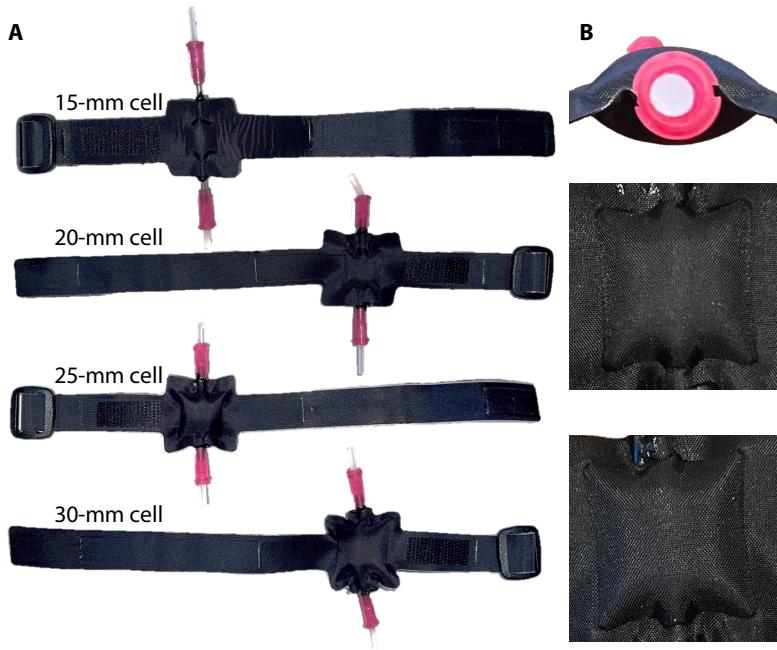
Figure S6. Each single-cell wristband after being filled with elastomer and cured under 1 bar of pressure. (**A**) The volumes of the cells (determined by weighing the elastomer cured within the wristbands) were used as a physical reference to determine the accuracy of our volumetric model such that the volume of the multi-cell module could be confidently used in the numerical model. (**B**) The 25-mm single-cell wristband cured while strapped to a user's wrist exhibits a symmetrical inflation (top) with no discernible difference between the sides that inflate toward (middle) or away from (bottom) the user's skin.

A

Volume [mL] vs Characteristic Length [mm]

- - - Maximum Volume
◆ Single-Cell Volumes

31.33 [mm], 5.86 [mL]

$$V_{max} = 0.190w^3$$

B
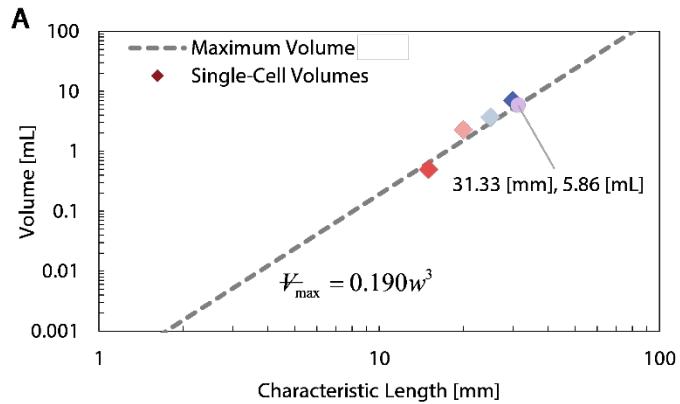
Figure S7. Modeled maximum volume of an arbitrarily sized inflated square plotted alongside the empirically determined volume of the textile cells. (**A**) Our cells match the expected volumetric function when filled with silicone elastomer at 1 bar of pressure. (**B**) The modified module is shown, filled with the elastomer. The measured volume is 17.58 mL for the entire module. When combining the volume of the cells and channels in the device, the average volume for the three cells becomes 5.86 mL, which puts the effective characteristic length of the cell at 31.3 mm as shown in (A).
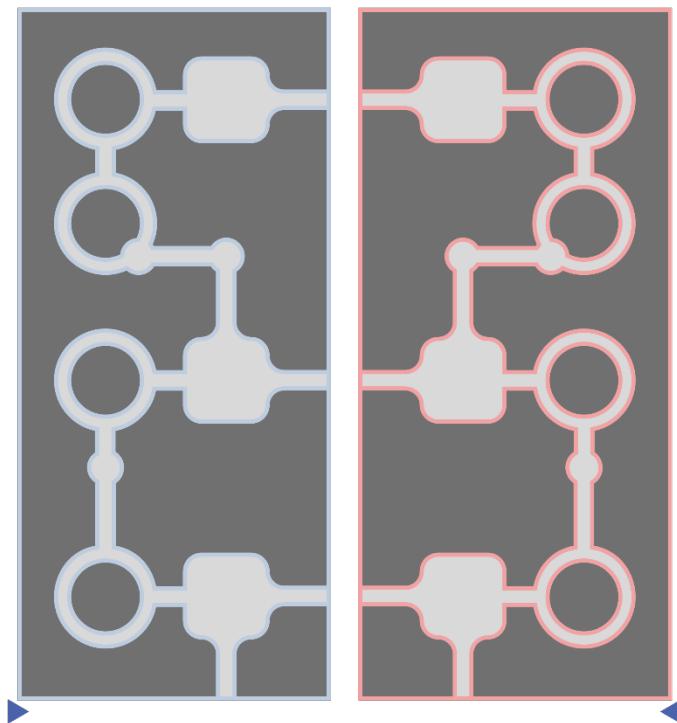
— 1st layer
— 2nd layer
▨ Heat-sealable textile (TPU-coated side facing up)
▢ Adhesive-backed paper
▲ Visual indicator for alignment

Figure S8. Cutting and assembling design for the modified fluidically controlled haptic textile module. The cells, channels, and locations where vias would have been are all the same dimensions as the original module but are moved to reside on two layers, rather than three. The exclusion of a third layer (and the resistors with negligible volumes) allows for the viscous elastomer to fill the entirety of the intermediate unbonded regions such that the device can be weighed for its volume at 1 bar of pressure.
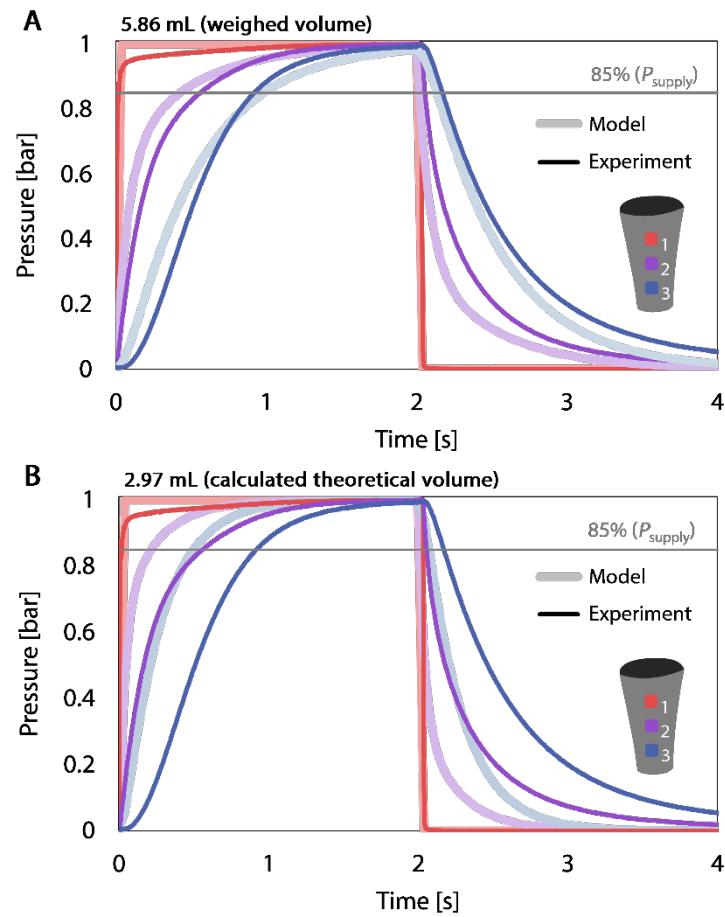
Figure S9. Numerical model accuracy relative to empirical data for different volumes of a cell. (**A**) The weighed volume shown in Figure S7 matches the experiment well, whereas the theoretical volume (for three 25-mm cells) from the model of a "tea bag" (**B**) neglecting the volume of the flow channels within the system causes the model to have errors on the same order of magnitude as the empirical data itself.
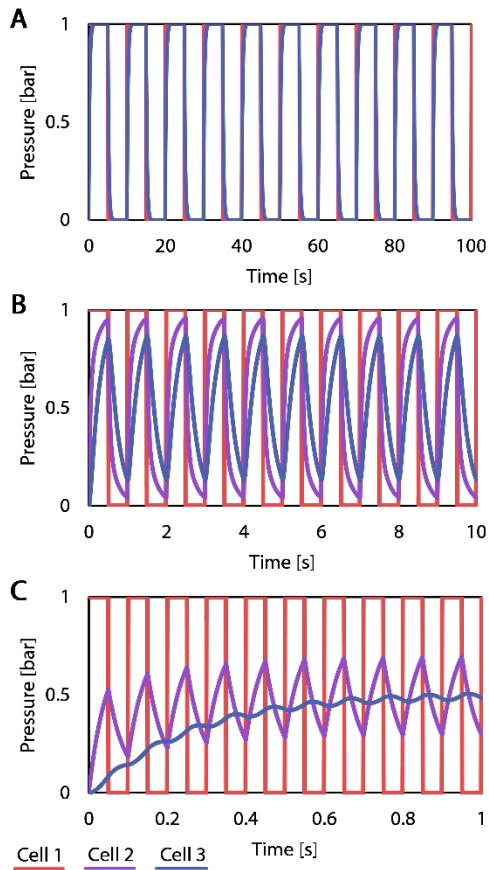
Figure S10. Modeled pressurization of fluidically programmed cells for a square waveform. Varying the oscillatory input across frequencies enables temporally distinct cues for each spatially distinct cell on the sleeve. At low frequencies, such as 0.1 Hz (**A**), all three cells closely follow the input waveform. At medium frequencies, such as 1 Hz (**B**), the successive cells exhibit attenuated amplitudes and phase lag, leading to different magnitudes of forces felt on the arm. At high frequencies, such as 10 Hz (**C**), the second cell exhibits significant attenuation but still mimics the input waveform, while the third cell approaches a nearly steady value.
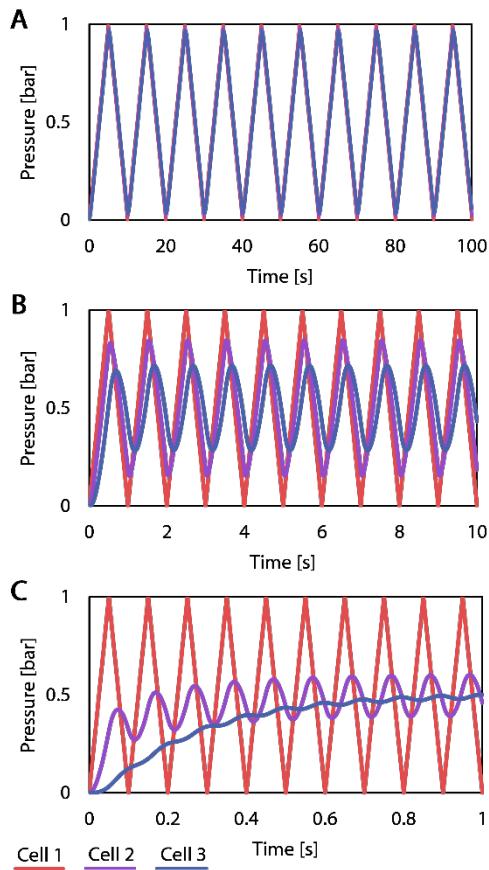
Figure S11. Modeled pressurization of fluidically programmed cells for a triangle waveform. Varying the oscillatory input across frequencies enables temporally distinct cues for each spatially distinct cell on the sleeve. At low frequencies, such as 0.1 Hz (**A**), all three cells closely follow the input waveform. At medium frequencies, such as 1 Hz (**B**), the successive cells exhibit attenuated amplitudes and phase lag, leading to different magnitudes of forces felt on the arm. At high frequencies, such as 10 Hz (**C**), the second cell exhibits significant attenuation but still mimics the input waveform, while the third cell approaches a nearly steady value.
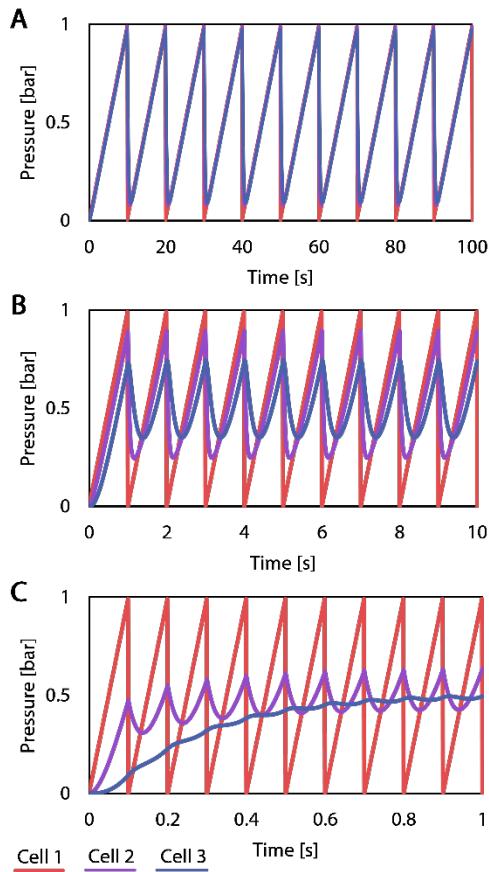
Figure S12. Modeled pressurization of fluidically programmed cells for a sawtooth waveform. Varying the oscillatory input across frequencies enables temporally distinct cues for each spatially distinct cell on the sleeve. At low frequencies, such as 0.1 Hz (**A**), all three cells closely follow the input waveform. At medium frequencies, such as 1 Hz (**B**), the successive cells exhibit attenuated amplitudes and phase lag, leading to different magnitudes of forces felt on the arm. At high frequencies, such as 10 Hz (**C**), the second cell exhibits significant attenuation but still mimics the input waveform, while the third cell approaches a nearly steady value.
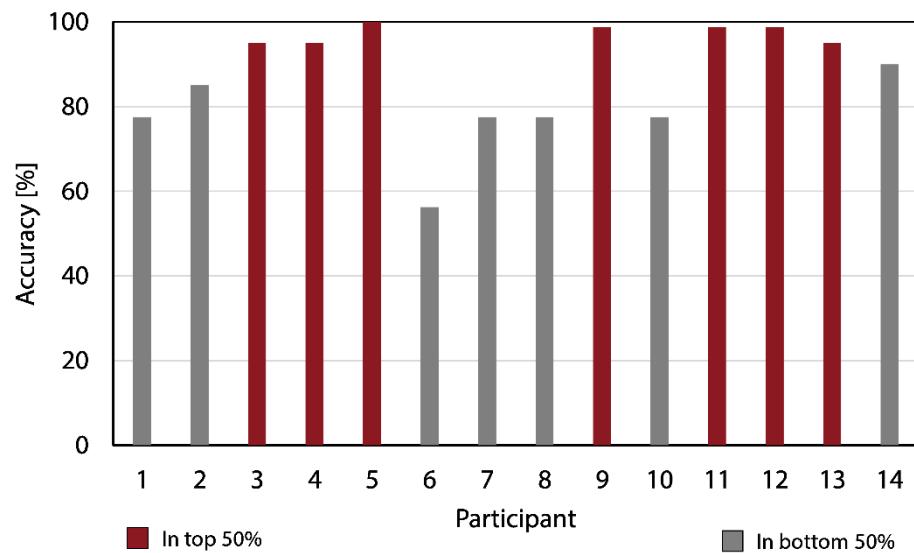
Figure S13. Average accuracy across all four types of cues (forward, backward, left, right) of each participant. The deviation in results between "non-responders" (bottom 50%) and "responders" (top 50%) substantiates the delineation between the groups. The deviation is shown in more detail in **Figure S14**.
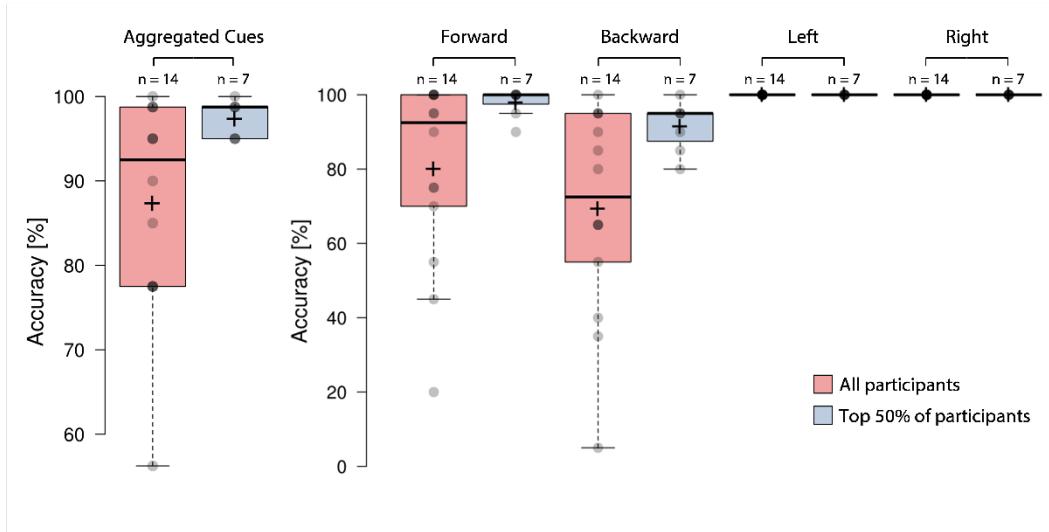
Figure S14. Accuracy of participants and for each type of directional cue. The accuracy of the participants is spread across two levels. Center lines show the medians; box limits indicate the 25th and 75th percentiles as determined by R software; whiskers extend 1.5 times the interquartile range from the 25th and 75th percentiles, outliers are represented by dots; crosses represent sample means; data points are plotted as open circles.
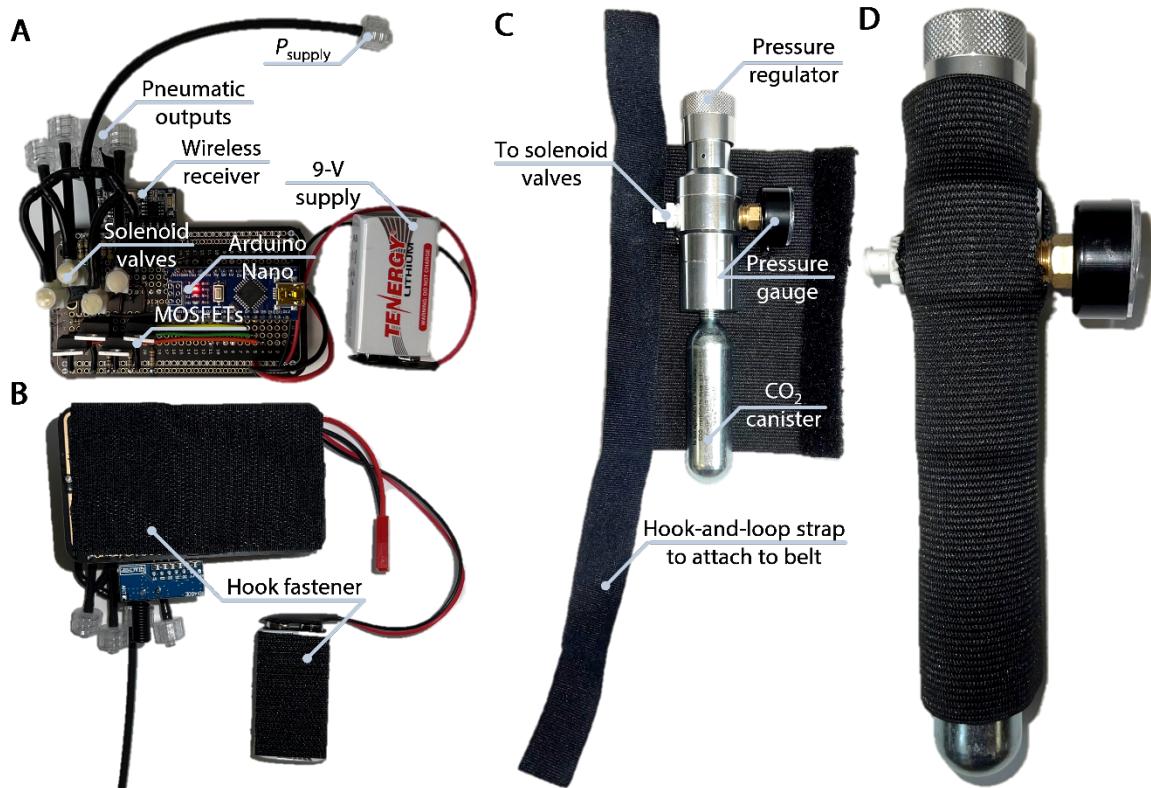
Figure S15. Close-up photographs of the belt-worn components for the untethered real-world demonstrations. (**A**) Custom protoboard with all electronic components (weighing 122 g) required for receiving wireless signals, controlling solenoids, and powering the electrical system. (**B**) Adhesive-backed hook fastener was bonded to the components in (A) for easy attachment to the elastic belt in Figures 6A and 6B. (**C**) Tailored elastic textile sleeve for pneumatic power supply such that it can be attached to the belt and prevent thermal discomfort from the Joule-Thomson effect and the pressure-cooking effect (where the ideal gas law dictates that releasing pressure from a vessel filled with liquefied gas drops the local temperature to its ambient boiling point). (**D**) Textile sleeve wrapped around pneumatic power supply as it would be when attached to the belt. The pneumatic supply weighs 223 g.

Figure S16. GPS data and target route for untethered walking navigation over 1 km of city streets. We trained the user to follow the direction that was perceived through the sleeve, that cues would be given approximately 5 m prior to each junction in the sidewalk, and that a backward cue indicated the end of the route. The user had 100% accuracy in perceiving the directional cues.
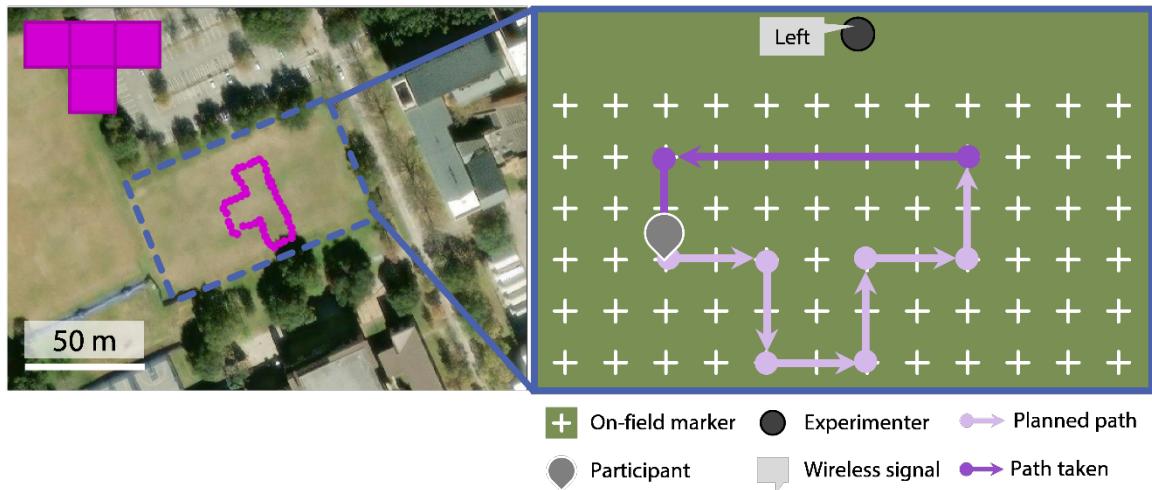
Figure S17. Experimental setup for untethered navigation demonstrated through walking the shape of polyominoes. On-field markers (spaced 7 m apart) created a cartesian coordinate system that allowed the experimenter to plan the path and the participant to orient their rotations to 90° when turning. The user was trained on the directional meaning of the spatiotemporal cues and was instructed to start each trial at a predefined initial coordinate. Walking at a normal pace, the experimenter wirelessly provided directional cues (forward, left, and right) approximately halfway between each cone or at the starting cone to initiate the trial. A backward cue indicated stopping and that the trial was over, and two backward cues indicated a 180° turn. The experimenter was physically distanced from the user in a tower that overlooks the field. In addition to the fact that the participant was not told the shapes at the beginning of each trial, we note that the participant claimed the inability to visualize or identify the shapes during or after finishing each trial, indicating the participant's reliance purely on the cues delivered by the haptic shirt rather than proprioceptive notions of their preceding moves during navigation.
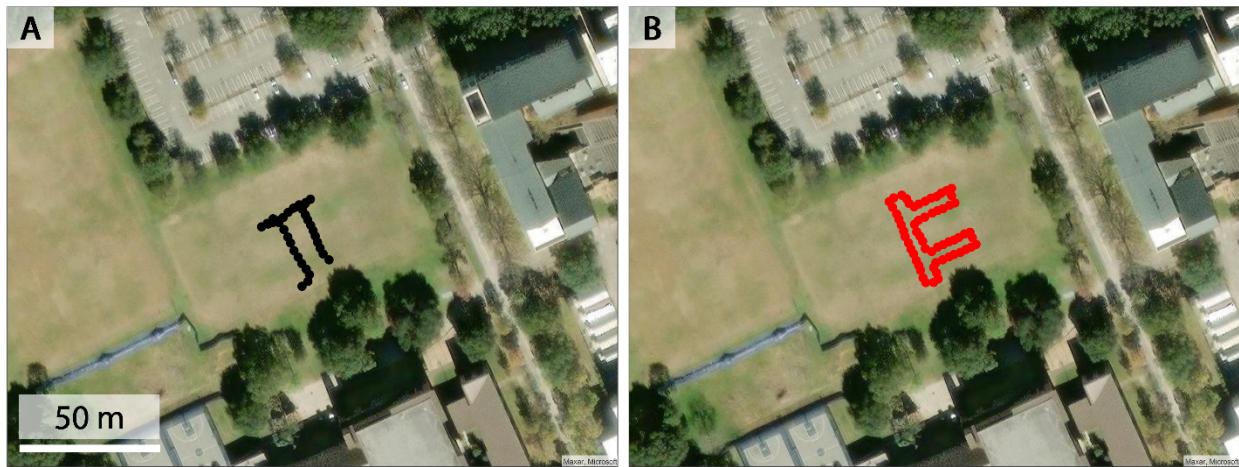
Figure S18. GPS data of the two Π symbols produced by the participant. (**A**) A text-like Π symbol shows that the participant could perform 180° turns ("U-turns") by perceiving two backward cues in rapid succession. (**B**) The participant also performed a polyomino Π symbol, shown in Movie S3.
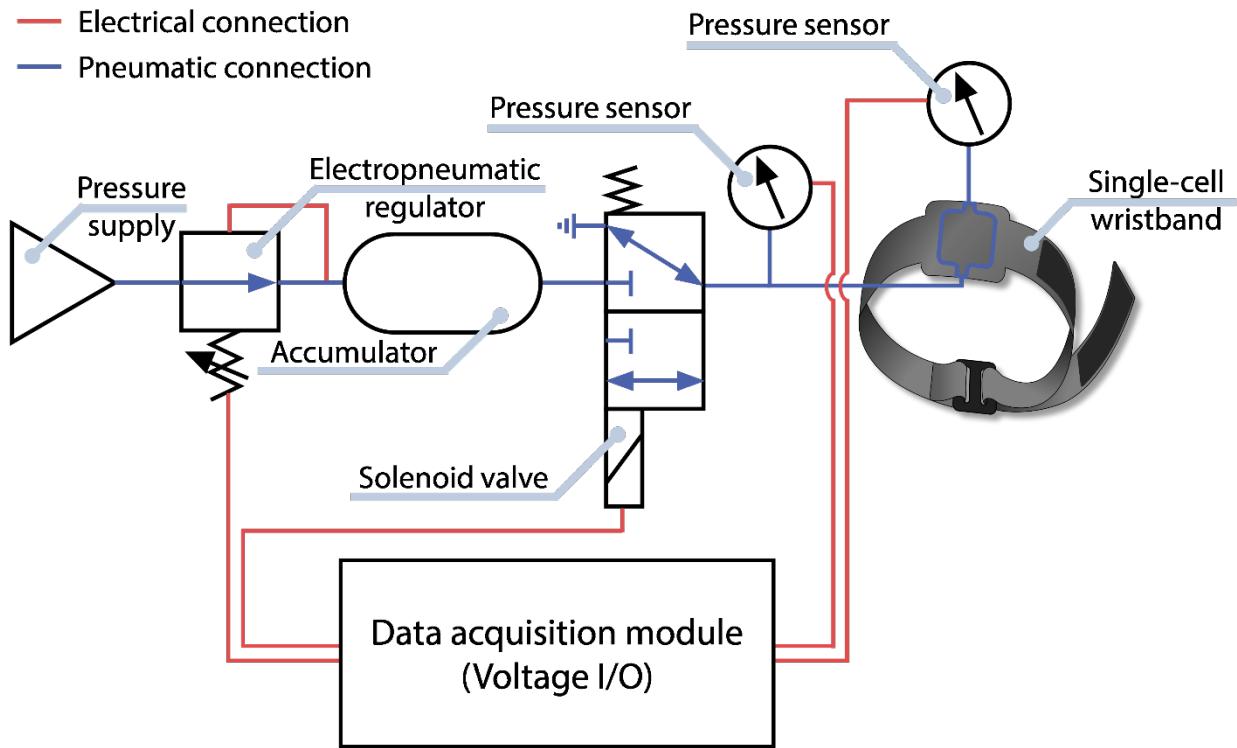
Figure S19. Schematic of the electropneumatic circuit for static analysis of the single-cell wristbands. Each wristband was wrapped around the instrumented test rig (Figure S3) and was measured for its tactile (normal) force based on the input fluidic pressure as controlled by the electromechanical system.
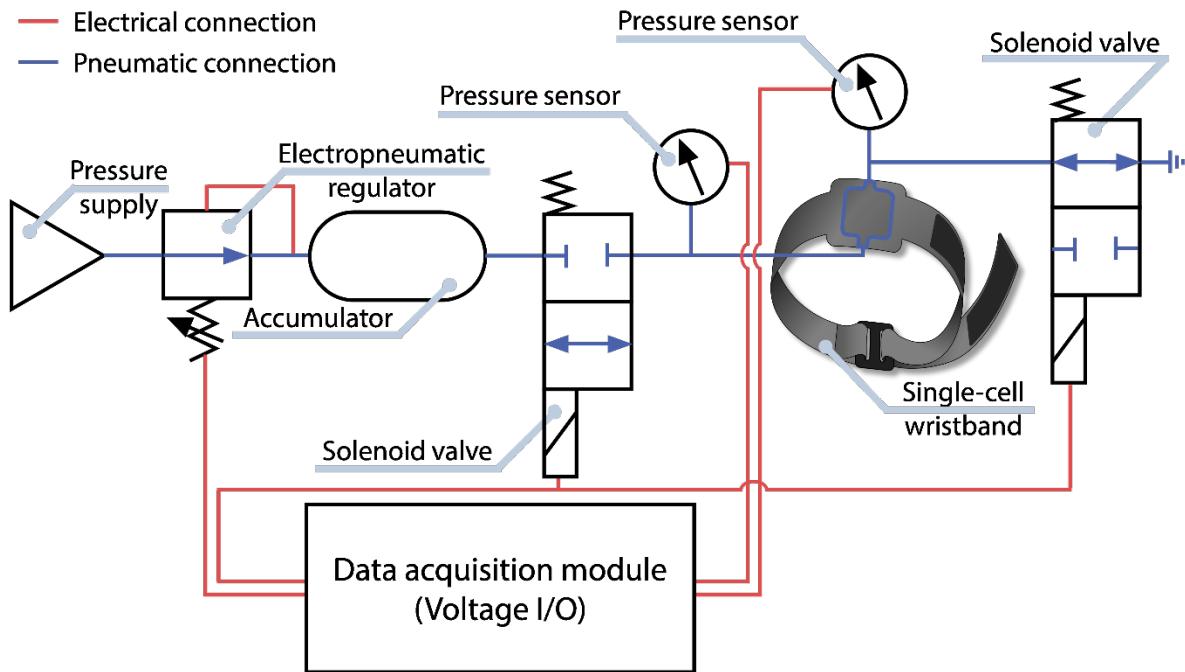
Figure S20. Schematic of the electropneumatic circuit for dynamic analysis of the single-cell wristbands. Each wristband was wrapped around the instrumented test rig (Figure S3) and was measured for its tactile (normal) force based on the input fluidic pressure as controlled by the electromechanical system. The setup shown here for dynamic analysis required two high-frequency solenoids, one for the inlet and one for the outlet due to the model of solenoid (SX12-AG, SMC Pneumatics).
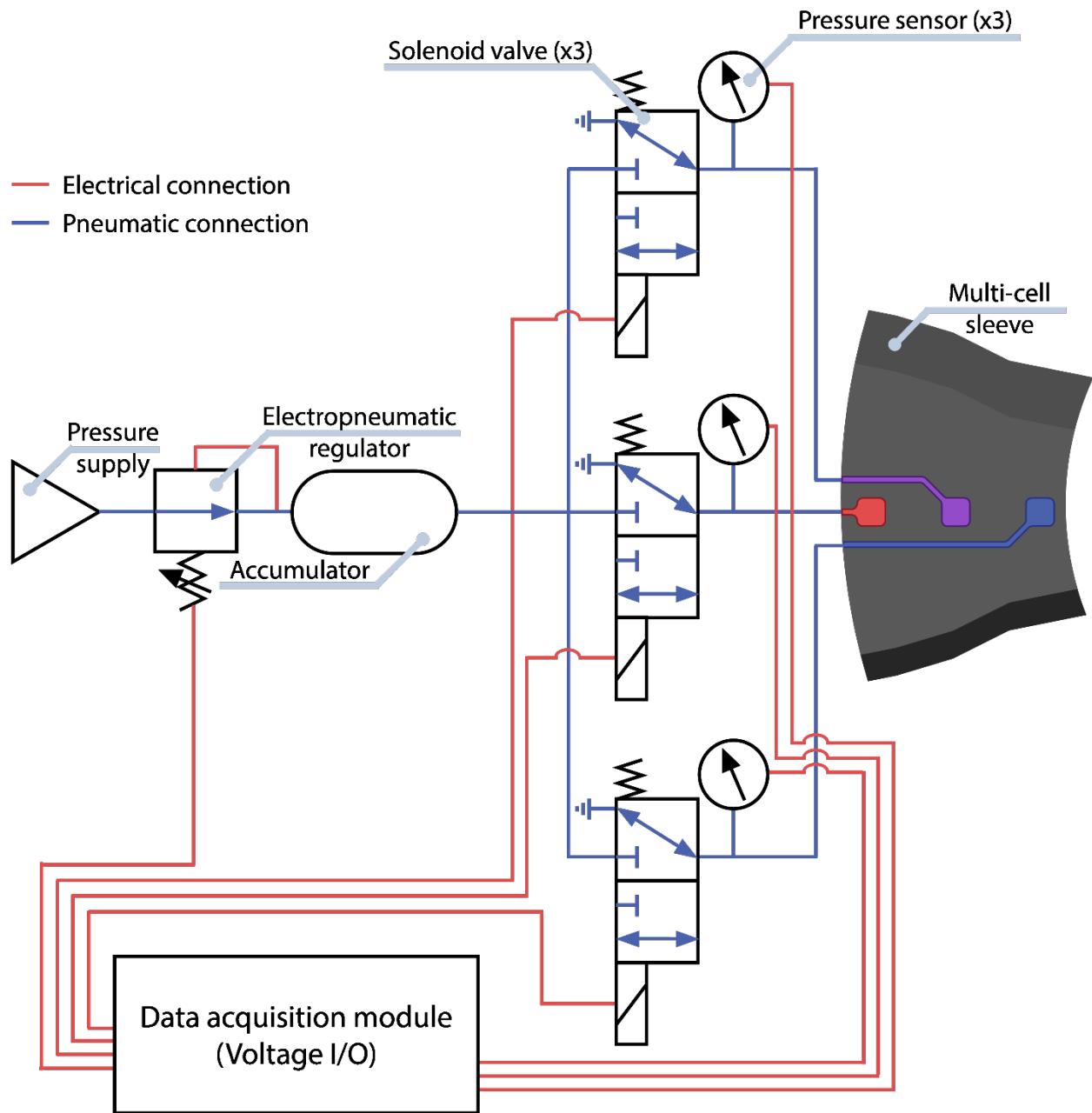
Figure S21. Schematic of the electropneumatic circuit for characterization of the multi-cell sleeve. This sleeve used three solenoid valves for individually addressable cells. In this manner, each cell could deliver a diverse array of spatiotemporal cues based on valve-based programming but would be encumbering to a user in a real-world scenario.
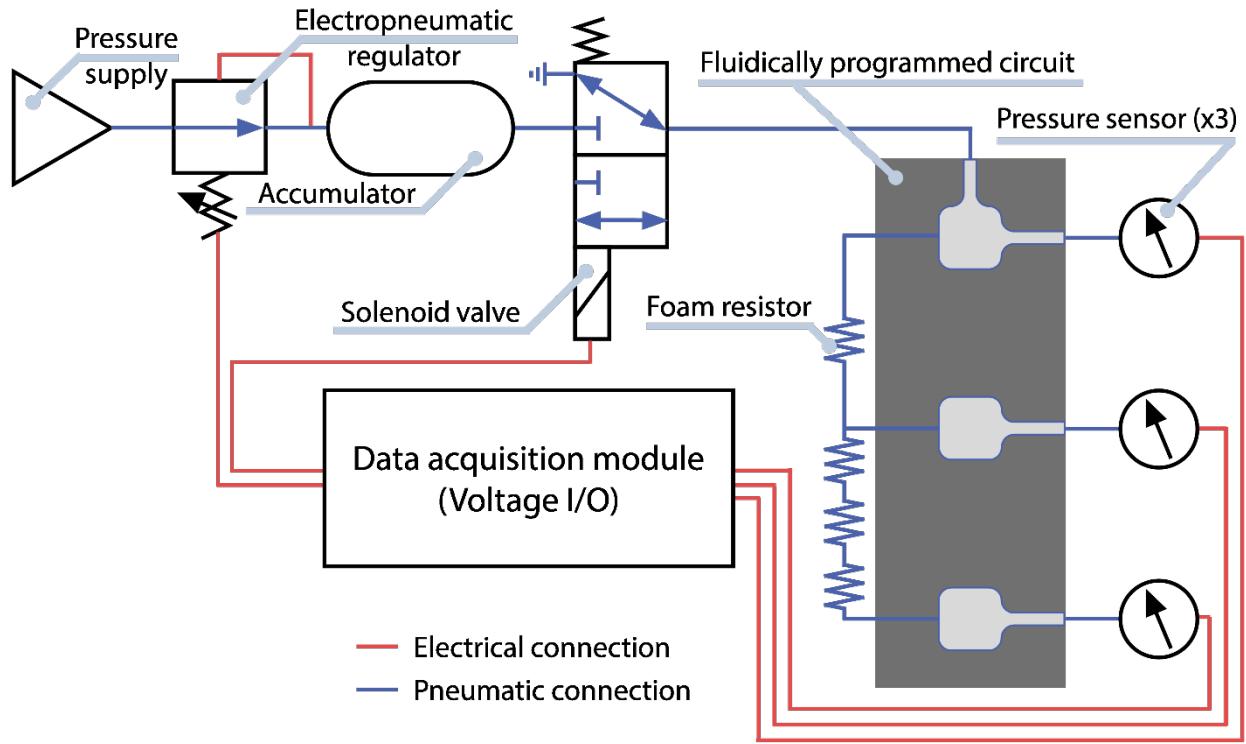
Figure S22. Schematic of the electropneumatic circuit for characterization of the fluidically programmed haptic textile module. The foam resistors were integrated directly into the textile as shown in Figure 4A but are shown here in a simplified schematic due to the three-layer composition of the module. The incorporation of a preprogrammed fluidic circuit allows for the reduction of accompanying electromechanical hardware, which enables more practical delivery of spatiotemporal cues in real-world settings.

1st layer

2nd layer

Heat-sealable textile (TPU-coated side facing up)

Adhesive-backed paper

Visual indicator for alignment
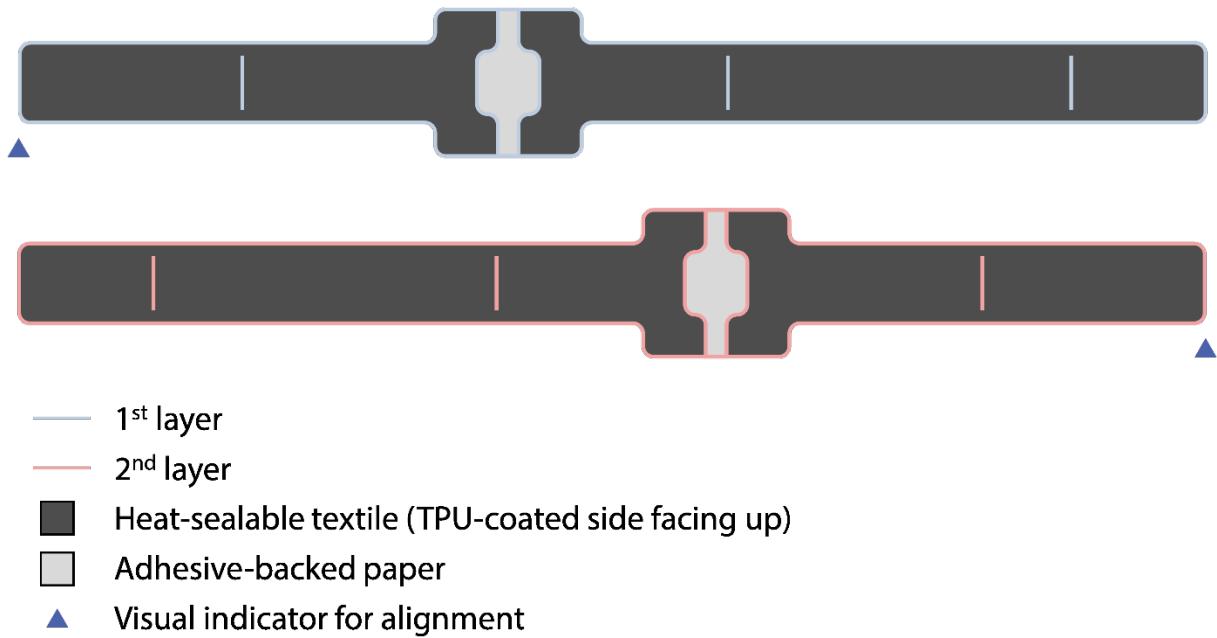
Figure S23. Cutting and assembling design for the 15-mm single-cell wristband. The vertical lines are for weaving a non-stick ribbon through the stacked layers such that their relative alignment is maintained during the heat pressing process. We used the residual backing of the adhesive-backed paper for this non-stick ribbon. The ribbon was then be trimmed after assembly.

- — 1st layer
- — 2nd layer
- ■ Heat-sealable textile (TPU-coated side facing up)
- □ Adhesive-backed paper
- ▲ Visual indicator for alignment
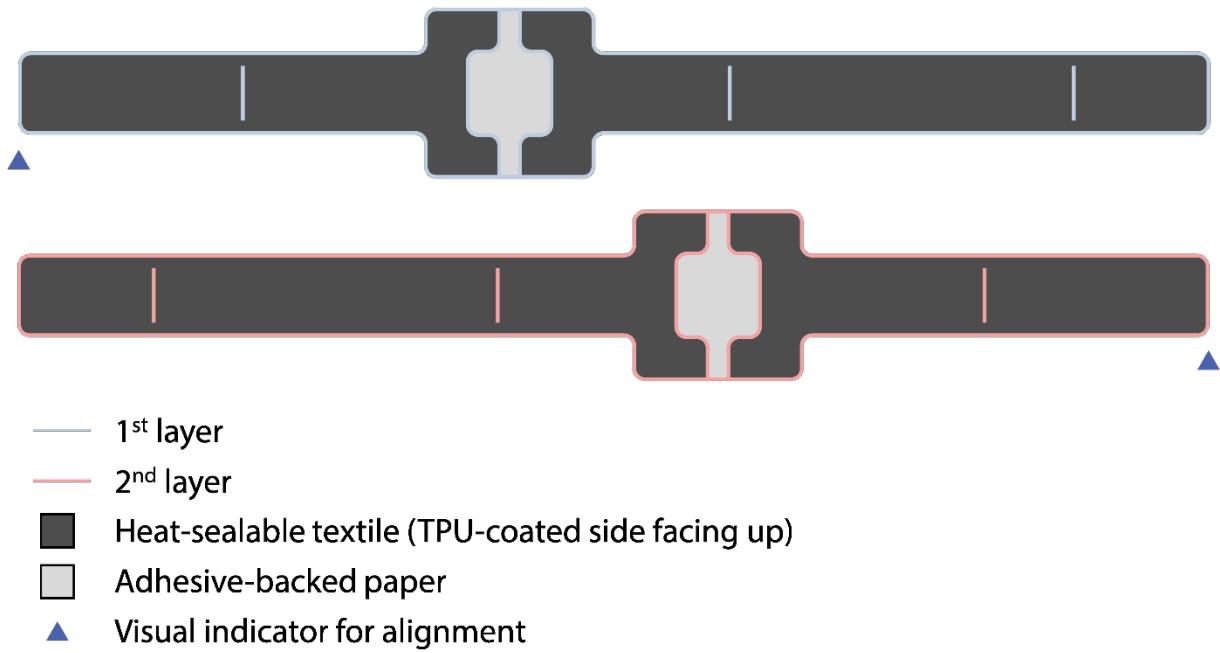
Figure S24. Cutting and assembling design for the 20-mm single-cell wristband. The vertical lines are for weaving a non-stick ribbon through the stacked layers such that their relative alignment is maintained during the heat pressing process. We used the residual backing of the adhesive-backed paper for this non-stick ribbon. The ribbon was then be trimmed after assembly.

— 1st layer
— 2nd layer
■ Heat-sealable textile (TPU-coated side facing up)
□ Adhesive-backed paper
▲ Visual indicator for alignment
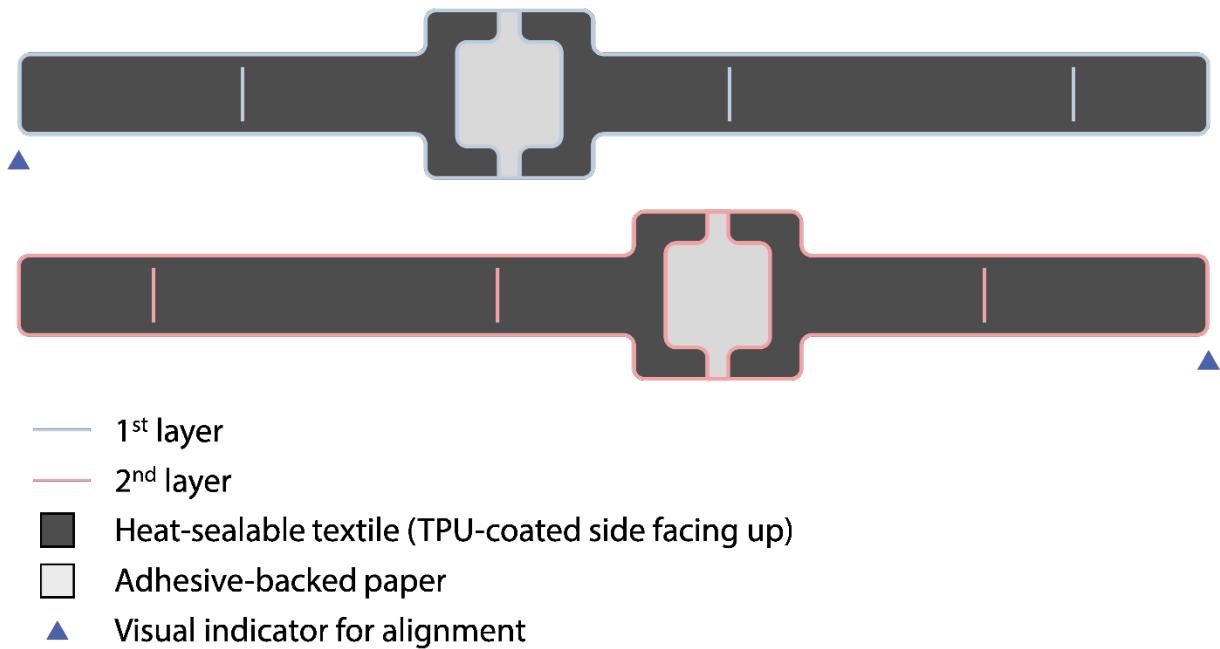
Figure S25. Cutting and assembling design for the 25-mm single-cell wristband. This 25-mm cell is the design used in the sleeves that provide spatiotemporal cues, based on the exhibited force-pressure relationship. The vertical lines are for weaving a non-stick ribbon through the stacked layers such that their relative alignment is maintained during the heat pressing process. We used the residual backing of the adhesive-backed paper for this non-stick ribbon. The ribbon was then be trimmed after assembly.

1st layer

2nd layer

Heat-sealable textile (TPU-coated side facing up)

Adhesive-backed paper

Visual indicator for alignment
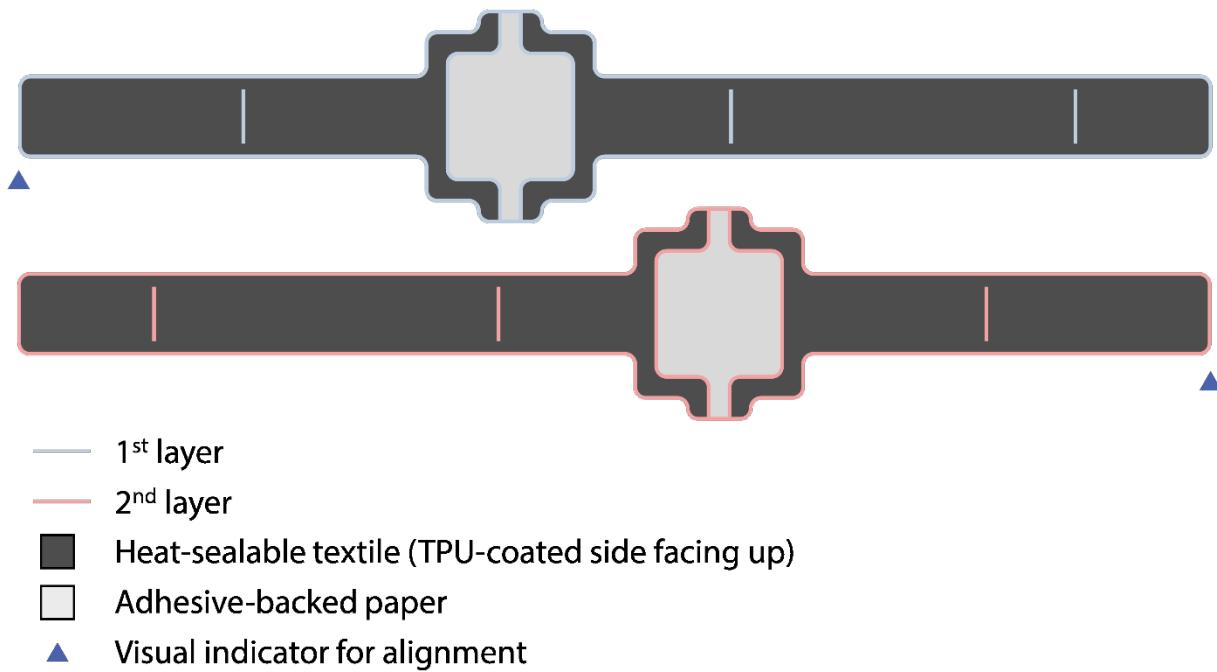
Figure S26. Cutting and assembling design for the 30-mm single-cell wristband. The vertical lines are for weaving a non-stick ribbon through the stacked layers such that their relative alignment is maintained during the heat pressing process. We used the residual backing of the adhesive-backed paper for this non-stick ribbon. The ribbon was then be trimmed after assembly.

Legend:

— 1st layer
— 2nd layer
······· Relative positioning of other layers
▪ Heat-sealable textile (TPU-coated side facing up)
□ Adhesive-backed paper
▨ Adhesive-backed hook-and-loop fastener
▲ Visual indicator for alignment
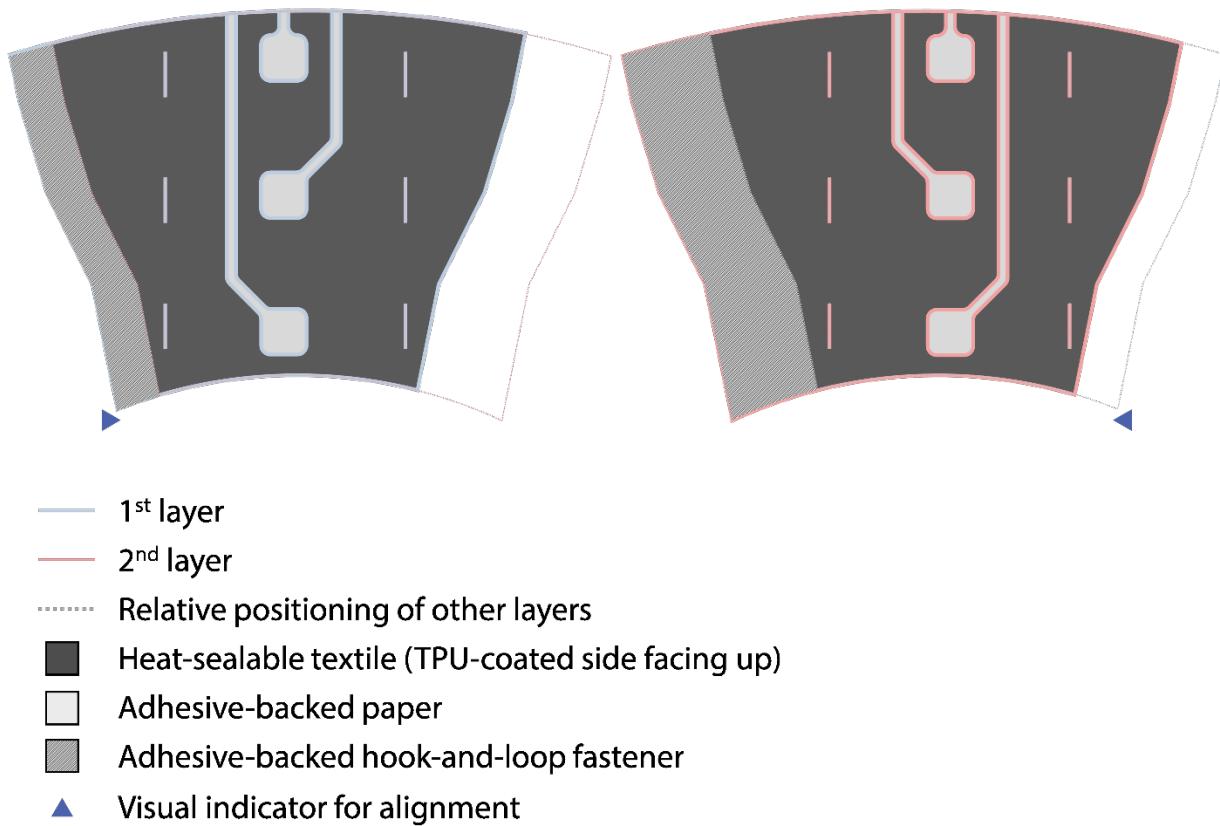
Figure S27. Cutting and assembling design for the multi-cell sleeve. We designed the sleeve to fit comfortably along the forearm with variable widths proportioned to the geometry of an author's forearm, and the hook-and-loop fasteners are wide enough to accommodate a large range of forearm sizes, as needed for human-subject testing.

Legend:

— 1st layer
— 2nd layer
— 3rd layer
...... Relative positioning of other layers
— · — Manual cut after assembly
■ Heat-sealable textile (TPU-coated side facing up)
□ Adhesive-backed paper
⊙ 22-mm (OD), 3-mm (ID) foam resistor
▲ Visual indicator for alignment
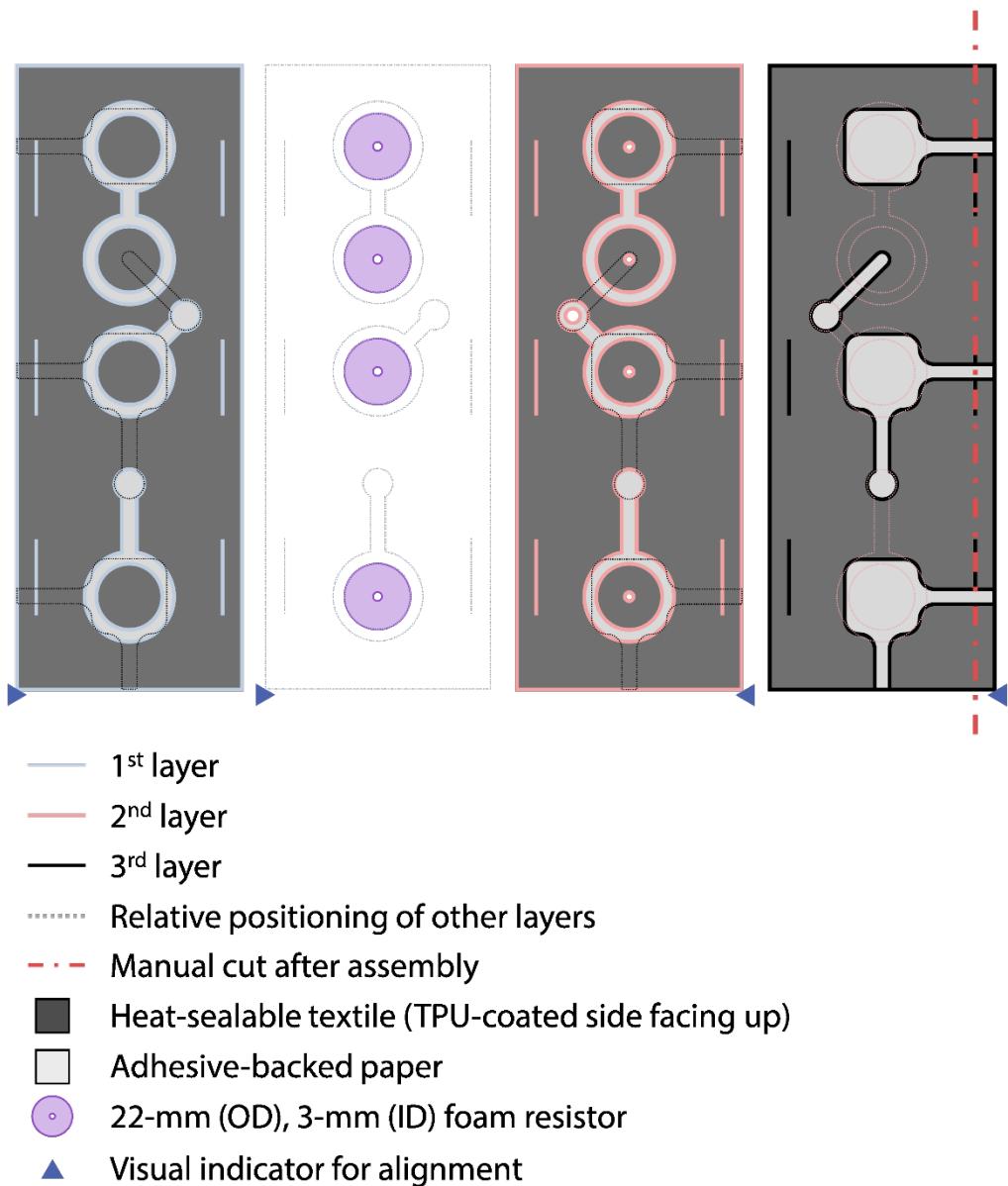
Figure S28. Cutting and assembling design for the programmed fluidic haptic module. The first step to create this device is to cut the textile layers. After aligning the three layers and loosely weaving the strip of non-stick material through the slits, the annular foam resistors were manually placed between the first and second layer. The thickness of the adhered paper aided in any misalignment of the foam resistors during thermal bonding.
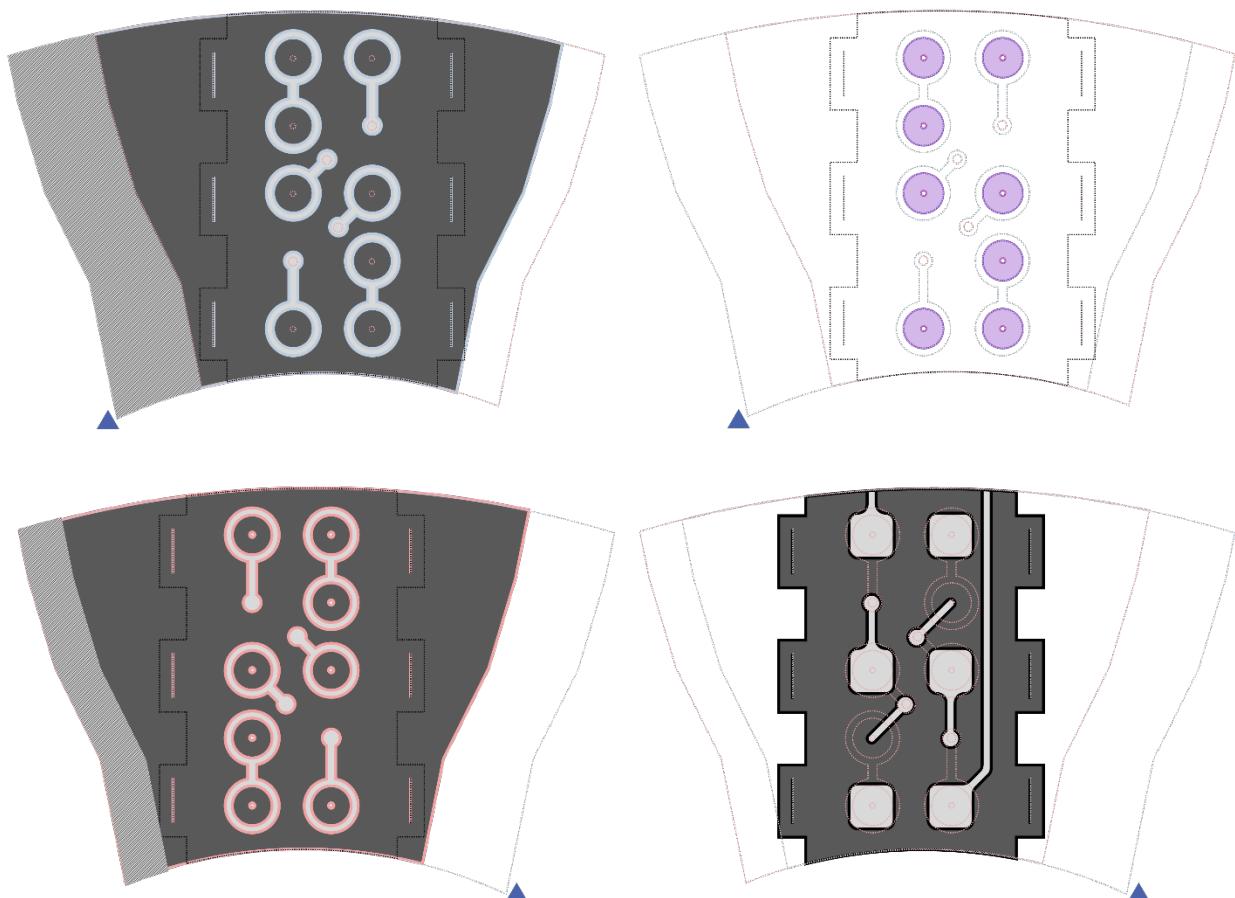
Legend:

- —— 1st layer
- —— 2nd layer
- —— 3rd layer
- ······ Relative positioning of other layers
- ▩ Heat-sealable textile (TPU-coated side facing up)
- ☐ Adhesive-backed paper
- ▨ Adhesive-backed hook-and-loop fastener
- ⊙ 22-mm (OD), 3-mm (ID) foam resistor
- ▲ Visual indicator for alignment

Figure S29. Cutting and assembling design for the navigational sleeves with spatiotemporal cues preprogrammed by textile-embedded circuits. The cutting and assembly processes are similar to that of the textile module with only one set of three cells. After aligning the layers and inserting the foam resistors, the device was thermally bonded. The aligning ribbon was trimmed, and adhesive-backed hook-and-loop fasteners were added to the opposing edges.

Supplemental Experimental Procedures

Fabrication and Design of Textile-Based Haptic Devices

The heat-sealable textiles (HSTs) used in this work are two-dimensional woven textile sheets coated with a thin film of thermoplastic polyurethane (TPU). Upon application of heat and pressure, the thin film of TPU reflows and, after cooling back below its melting temperature, adheres to an opposing surface. In this manner, a layer of HST can form a thermal bond with other fabrics (including the uncoated side of another HST) or to other TPU films or coatings. The introduction of an impermeable intermediate layer that prevents thermal bonding defines internal pathways between textile sheets through which fluid may flow.

After thermally bonding two or more layers of HSTs, the resulting construction forms a durable yet compliant mechanical transducer of fluids. The process we outline here for fabricating our devices from HSTs is cost-effective and can be almost entirely automated (**Figure S2B**), unlike many existing manufacturing methods of soft devices. The single-cell wristbands are sized approximately to the dimensions of a "smart watch" (a commercially available wearable haptic device) and can be similarly adjusted to a preferred tightness. Our wristbands attach to the user with hook-and-loop fasteners (9273K13, McMaster-Carr) sewn or adhered to the straps, and the wristband can be tightened by feeding the straps through a sewn-in slide bracket (2974T45, McMaster-Carr). The multi-cell sleeves use wider strips of adhesive-backed hook-and-loop fasteners (9273K16, McMaster-Carr) to fit a variety of forearms. We fabricated all textile haptic devices with similar methods and materials.

The process of fabrication starts with a rough-cut sample of 70-denier nylon taffeta (FHST, Seattle Fabrics), with the TPU-coated side facing up, placed on an adhesive mat (X1224PLC3, XINART) that can be fed into the vinyl cutter (Cricut Maker [2005464], Cricut). We then applied the adhesive-backed paper (DL8511FS, Packzon) to the topside of the HST and inserted the mat into the vinyl cutter. The first cutting operation used the "Washi Sheet" material setting with pressure modified to "less" in the Cricut Design Space software. This cut patterned the masking layer (the adhesive-backed paper) to define the internal geometries where the HST will not bond and thus allow fluid to flow and pressurize between layers. The second cutting operation defined the outline of the textile by cutting through both the textile and paper layers with the material setting set to "Light Cardstock" modified to have "more pressure." Both cutting operations used a fine-point blade (LWW-Cricut blades-40p, Luxiv). The layer-by-layer designs of each device can be found in **Figures S23–S29**.

After both cuts were completed, the mat was removed, and the excess material was weeded away. We stacked the layers together in their respective order, often with the TPU-coated sides facing each other (except for the three-layer devices, such as the resistor-integrated module and sleeves with textile-embedded fluidic programming, which had their cell-defining layer placed with the TPU-coated side facing the textile side of the resistive layers). The layers were aligned with each other and held together by weaving strips (cut from the backing sheet of the adhesive-backed paper) through slits cut into the periphery of the devices, such that the layers would not shift relative to each other when thermally bonded. If the device required resistors, we placed the annular resistors between layers after alignment but prior to bonding. The resistors were made from 1.6-mm-thick (1/16-inch) open-cell polyurethane foam (86375K132, McMaster-Carr) cut from a concentric hollow punch (66004, Mayhew Steel Products).

We thermally bond the layers at 200° C for 30 s using a DK20SP (Geo Knight & Co) heat press, set to 345 kPa. Promptly after heat pressing, we placed the device into a separate room-temperature manual press (JetPress 12, Geo Knight & Co) acting as a thermal sink for 30 s to isothermally cool (akin to quenching) the TPU under pressure while still aligned by the interwoven strips. This "quenching" process was not performed for devices with foam resistors integrated between layers because the layers would cool around the compressed resistors and affect their fluidic resistance.

Once the bonding process was completed, we trimmed the strips woven through the slits for alignment. After applying the hook-and-loop fasteners, Luer lock twist-to-connect dispensing tips (JG13-0.5HPX, Jensen Global) pneumatically coupled the air supply and the textile device. The couplers were affixed to the inlets of the textile devices with either fabric glue (FBA_FS-12, Surebonder) using a high-temperature hot glue dispenser (BS778, Boswell) or a two-part epoxy (50139 Plastic Bonder, J-B Weld) to form a hermetically sealed joint.

Instrumented Test Rig

To capture the forces imposed by our wristbands, we approximated the anatomical proportions and geometry of a wrist in a computer-aided design (CAD) program (**Figure S3A**). We segmented the wrist into inner and outer portions. The inner portion consisted of a "skeletal" structure additively manufactured from a material-jetting 3D printer (ProJet MJP 2500, 3D Systems) using a rigid resin (VisiJet-M2R-CL, 3D Systems). The bending modulus for the resin is reported as 1.7–2.2 GPa, while the radius and ulna bones have respective bending moduli of 3.7 GPa and 4.5 GPa.[8] The center of the inner structure also contains a hollow location for a load cell placed below a plate to evenly distribute applied loads.

The outer portions (intended to emulate human tissue) were redesigned into a mold, which was also additively manufactured by a 3D printer (ProJet MJP 2500, 3D Systems) using the same resin (VisiJet-M2R-CL, 3D Systems). We mixed (in a 1-to-1 ratio) a two-part platinum-catalyzed silicone elastomer (Ecoflex 00-30, Smooth-On) and cast the uncured solution into the molds. The silicone cured at room temperature for the prescribed amount of time (> 4 hours). After curing, the elastomer is reported to have an elastic modulus of 1.4 MPa, matching closely with the elastic modulus of human skin, 1.2 MPa.[9]

With a 6-axis load cell (Nano 25, ATI – Industrial Automation) placed endogenously in the rigid inner structure, we fastened the inner and outer portions together. The instrumented wrist rig was secured to an optical breadboard with ¼"-20 bolts, placed within close proximity to the pneumatic components necessary for each experiment. Further experiments using this instrumented wrist rig and the details thereof can be found in prior works by the co-authors.[10–15]

Captions for Supplemental Movies

Movie S1. Programming Spatiotemporal Cues in a Wearable Sleeve. Operation of spatiotemporal cues within fluidic haptic textiles: multi-cell sleeve with valve-based programming, module with fluidically programmed spatiotemporal cues, and sleeves capable of directional cues through the combination of fluidically programmed cues.

Movie S2. Integrating Haptic Cues into an Untethered Wearable Format for In-the-Wild Navigation. Untethered navigation by a user walking and operating a scooter with fluidically programmed haptic sleeves integrated into a shirt and electrical components mounted on a belt.

Movie S3. Drawing Tetrominoes in an Open Field. Untethered "drawing" of tetrominoes based on the walking path of a user in an open field guided by fluidically programmed directional cues delivered by wirelessly transmitted signals.

Movie S4. Robustness of the System. Demonstrated robustness of fluidically programmed wearable haptic textiles in two real-world scenarios: (i) washing 25 times and (ii) repairing a punctured cell with a household iron.

Supplemental References

1. Weisstein, E.W. Paper Bag Surface. https://mathworld.wolfram.com/.
2. Mladenov, M.I. (2001). On the Geometry of the Mylar Balloon. Comptes Rendus de l'Academie Bulgare des Sciences *54*, 9.
3. Paulsen, W.H. (1994). What Is the Shape of a Mylar Balloon? The American Mathematical Monthly *101*, 953–958. 10.2307/2975161.
4. Gammel, A. (2011). The Teabag Constant. Gammel Puzzel Page. http://web.archive.org/web/20110527161001/http://www.dse.nl/~andreas/teabag.html.
5. Finch, S.R. (2003). Inflating an Inelastic Membrane. In Mathematical Constants II (Cambridge University Press), pp. 747–750.
6. Pruett, H., and Hyatt, L. (2019). Approximating Deformation of Inflatable Tubules Using Poisson's Equation. Journal of Applied Engineering Mathematics *6*.
7. Robin, A.C. (2004). Paper Bag Problem. Mathematics today.
8. Singh, D., Rana, A., Jhajhria, S.K., Garg, B., Pandey, P.M., and Kalyanasundaram, D. (2019). Experimental Assessment of Biomechanical Properties in Human Male Elbow Bone Subjected to Bending and Compression Loads. Journal of Applied Biomaterials & Functional Materials *17*, 2280800018793816. 10.1177/2280800018793816.
9. Ní Annaidh, A., Bruyère, K., Destrade, M., Gilchrist, M.D., and Otténio, M. (2012). Characterization of the Anisotropic Mechanical Properties of Excised Human Skin. Journal of the Mechanical Behavior of Biomedical Materials *5*, 139–148. 10.1016/j.jmbbm.2011.08.016.
10. Pezent, E., O'Malley, M.K., Israr, A., Samad, M., Robinson, S., Agarwal, P., Benko, H., and Colonnese, N. (2020). Explorations of Wrist Haptic Feedback for AR/VR Interactions with Tasbi. In Extended Abstracts of the 2020 CHI Conference on Human Factors in Computing Systems CHI EA '20. (Association for Computing Machinery), pp. 1–4. 10.1145/3334480.3383151.
11. Pezent, E., Israr, A., Samad, M., Robinson, S., Agarwal, P., Benko, H., and Colonnese, N. (2019). Tasbi: Multisensory Squeeze and Vibrotactile Wrist Haptics for Augmented and Virtual Reality. In 2019 IEEE World Haptics Conference (WHC), pp. 1–6. 10.1109/WHC.2019.8816098.
12. Pezent, E., Agarwal, P., Hartcher-O'Brien, J., Colonnese, N., and O'Malley, M.K. (2022). Design, Control, and Psychophysics of Tasbi: A Force-Controlled Multimodal Haptic Bracelet. IEEE Transactions on Robotics, 1–17. 10.1109/TRO.2022.3164840.
13. Jumet, B., Zook, Z.A., Xu, D., Fino, N., Rajappan, A., Schara, M.W., Berning, J., Escobar, N., O'Malley, M.K., and Preston, D.J. (2022). A Textile-Based Approach to Wearable Haptic Devices. In 2022 IEEE 5th International Conference on Soft Robotics (RoboSoft) (IEEE), pp. 741–746. 10.1109/RoboSoft54090.2022.9762149.
14. Fino, N., Jumet, B., Zook, Z.A., Preston, D.J., and O'Malley, M.K. (2023). Mechanofluidic Instability-Driven Wearable Textile Vibrotactor. IEEE Transactions on Haptics, 1–6. 10.1109/TOH.2023.3271128.
15. Pezent, E., Macklin, A., Yau, J.M., Colonnese, N., and O'Malley, M.K. Multisensory Pseudo-Haptics for Rendering Manual Interactions with Virtual Objects. Advanced Intelligent Systems *n/a*, 2200303. 10.1002/aisy.202200303.